SUPPLEMENTARY INFORMATION

Table of contents

I Structural characterization

When tackling such a difficult sample synthesis procedure, samples characterization is pivotal. The possible structures of Lanthanum hydrides at Mbar pressures have been studied in experimental [Laniel et al. 2022] as well as purely theoretical structural search works [Peng et al. 2017; Shipley et al. 2020; Errea, Belli, et al. 2020]. In this wide literature, the phase most commonly recognized to be stable and that show strong SC behavior displays a $Fm\bar{3}m$ space-group symmetry [Drozdov et al. 2019; Liu et al. 2018]. This comprises a cubic close-packed fcc structure of La atoms, that are arranged in triangular layers with an ABC stacking along the [111] direction of the conventional cubic cell (as shown in **Extended Data Fig. 6**, top left panel). The much smaller H atoms occupy the interstitial positions of such highly symmetric close-packed lattices. Hydrogen atoms can be symmetry-wise grouped in two sets of Wyckoff positions, $8c$ and $32f$: the former are located at tetrahedral interstitial positions, the latter instead arrange in regular cubes at octahedral interstitial sites or in regular tetrahedra around the $8c$ Hydrogen at tetrahedral sites. As a result, they form a cage around each La atom that can be seen as a chamfered cube, a highly symmetric convex polyhedron with 6 congruent squares and 12 congruent flattened hexagons having two internal angles of $109.47°$ and the remaining four of $125.26°$ (**Extended Data Fig. 6**, bottom left). We will refer to this highly symmetric phase as fcc-LaH_{10}. Several other structural phases have been proposed, including rhombohedral $R\bar{3}m$, orthorhombic $Immm$ and monoclinic C_2 or C_2/m ones [Errea, Belli, et al. 2020; Sun et al. 2021] [Eremets et al. 2022]. All such phases retain the ABC stacking of La triangular layers and can be seen as a symmetry-lowering deformation of the cubic close-packed fcc structure mostly involving a rearrangement of the hydrogen atoms and a consequent deformation of the chamfered-cubic cage.

A fundamentally different and competing hexagonal phase with $P6_3/mmc$ space-group symmetry and two formula units has been also proposed as thermodynamically stable and hosting a high-T_c superconducting phase [Shipley et al. 2020]: signatures of this structural phase have been reported as impurities in otherwise cubic structures [Drozdov et al. 2019; Sun et al. 2021]. In this structure La atoms form an hexagonal closed-packed (hpc) lattice where La triangular layers display a different ABAB stacking along the hexagonal c axis, that can be related to the fcc structure by a 3-fold rotation of the C layer about an axis orthogonal to the triangular layers and passing through a La atom (see **Extended Data Fig. 6** top panels). Hydrogen atoms can be grouped in three sets of Wyckoff positions of the highest-symmetric hexagonal $P6_3/mmc$ space group, namely $4e$, $4f$ and $12k$. Here the $4f$ H atoms sit at the center of tetrahedral interstitial sites while $4e$ and $12k$ H atoms form both distorted tetrahedra around $4f$ positions and distorted cubes filling the octahedral voids of the hpc lattice. The resulting substantial deformation of the hydrogen cage around each La atom can also be interpreted as a deformation of the chamfered cube where the lower half of the polyhedron with respect to the triangular-layer plane is rotated by $120°$ about a perpendicular axis passing through the La atom at the center of the H cage (**Extended Data Fig. 6**, bottom right panel). Nonetheless, the $P6_3/mmc$ phase displays the largest number of symmetries within the hexagonal crystal systems; henceforth we will refer to it as the hpc-LaH_{10} phase. Symmetry-lowering rearrangements of H atoms can be foreseen also for this hpc lattice, in close analogy with the several proposed modification of the fcc phase, that to the best of our knowledge have not been explored so far.

The different arrangement of La atoms in fcc and hcp lattices results in a clear identification of a hexagonal structure of La atoms from X-ray diffraction measurements, that instead cannot provide information on the Hydrogen positions due to its small atomic mass. Nonetheless, useful structural information can be extracted from Raman spectra, especially in the low-frequency range where vibrational signatures are mostly contributed by La phonons. La atoms do not contribute to any Raman-active phonon mode in the highly symmetric fcc $Fm\bar{3}m$ phase. On the other hand, the highly symmetric $P6_3/mmc$ phase allows for a single Raman-active La phonon, contrasting the structured spectra we observe in the 100-200 cm^{-1} frequency range. The latter observation, alongside the XRD characterization of the La hexagonal lattice, suggests a substantial rearrangement of Hydrogen atoms that may cause an overall symmetry reduction with a consequent activation of other La phonon modes. We explored this possibility by performing first-principles calculations of the candidate structures within density functional theory (DFT) using the generalized gradient approximation (GGA) as parametrized by Perdew, Burke and Ernzerhof (PBE) [Perdew et al. 1996].

Harmonic phonon frequencies were calculated within density functional perturbation theory (DFPT) [Baroni et al. 2001] making use of the Quantum ESPRESSO code [Paolo Giannozzi et al. 2009; Giannozzi et al. 2017]. We used optimized norm-conserving Vanderbilt pseudopotentials [Hamann 2013] from the Pseudo dojo repository [van Setten et al. 2018], including 11 electrons for La, with a plane-wave cut-off energy of 110 Ry for the kinetic energy. We adopted Γ-centered Monkhorst–Pack grid of k-points with a spacing of ~ 0.13 Å^{-1} and a Gaussian smearing of 0.03 Ry for Brillouin-zone integration. For structural optimization we adopted convergence criteria such that forces on the atoms were less than 2.5 meV Å^{-1} and stresses were less than 0.01 GPa. The static and dynamic phonon frequencies were obtained diagonalizing the dynamical matrix in these two limits as defined in the method and we tested a posteriori the negligible difference between static and dynamic eigen-vectors.

We first optimized the $P6_3/mmc$ structure previously reported [Shipley et al. 2020] at a classical pressure of 135 GPa, as quantum effects have been shown to add around 10-15% of extra pressure [Errea, Belli, et al. 2020; Errea, Calandra, et al. 2016; Belli and Errea 2022]. The calculated lattice parameters are $a = 3.72$ Å and $c = 5.68$ Å, roughly within 1% error with respect to refined XRD lattice constants (structural details are given in **Supplementary Table 1**). The enthalpy of such structure is 4.1 meV/f.u. above that of the fcc phase evaluated at the same pressure. We calculated the phonon dispersion by Fourier-interpolating the harmonic force constants on a 2×2×2 grid comprising the high-symmetry points Γ, A, L and M of the hexagonal Brillouin zone. Several phonon modes display imaginary frequencies, shown as negative values in Supplementary Figure **Supplementary Figure 1**: projection onto the La atomic character clearly shows that unstable modes mostly involves light H atoms, while La atoms mostly contribute to phonon modes in the 0–250 cm^{-1} range. As materials rich in light elements are sensible to quantum anharmonic effects, typically reducing the tendency to dynamical instabilities, we recalculate La-dominated phonon frequencies by artificially reducing the hydrogen atomic mass, thus disentangling the H contribution to those phonon modes**Supplementary Figure 2**. At the Γ point of the $P6_3/mmc$ (displaying D_{6h} point-group symmetries) there are only two optical phonon modes due to the La vibrations, among which only the E_{2g} (Γ_5^+ in the Miller-Love notation) mode at approximatively 90 cm^{-1} is Raman-active, as shown in Fig. **Supplementary Figure 2a**. The most unstable hydrogen phonon is a M_2^+ mode at M point of the hexagonal Brillouin zone (B_{1g} using the Mulliken notation for the D_{2h} point group of point M), that could lead to a 2×1×1 reconstruction with orthorhombic $Pnma$ structure or to a 2×2×1 hexagonal $P6_3/m$ phase comprising eight formula units. Interestingly, La-derived phonon modes appear in the frequency range 120-200 cm^{-1} at the M point, that might induce additional Raman-active modes when folded at the center of the Brillouin zone after the symmetry-lowering reconstruction (see coloured area in Fig. **Supplementary Figure 2a**). We discard the 2×1×1 orthorhombic reconstruction as it will turn on the Raman activity of the zone-center La phonon B_{1g} at $\sim$ 250 cm^{-1}, falling outside the targeted frequency range. Following the symmetry-lowering phonon mode M^{2+} we therefore optimized the hexagonal $P6_3/m$ structure and found an enthalpy gain of -2.8 meV/f.u. over fcc-LaH_{10}. In the reconstructed structure La atoms undergo very tiny displacements (at most of 4×10^{-3} Å) from the ideal positions of the $P6_3/mmc$ phase, while Hydrogen displacements are one order of magnitude larger. We computed phonon frequencies of the reconstructed cell limiting the calculations to inversion-even modes, i.e., those that may display Raman activity, in order to reduce the computational burden in such a large supercell. The zone-center Γ_5^+ mode of undistorted hpc-LaH_{10} is blue-shifted to $\sim$102 cm^{-1}, while other zone-folded phonon modes appear to become Raman-active in the frequency range between 100 and 200 cm^{-1} as shown in Fig. **Supplementary Figure 2b**. Among these, we identify those contributing to satellite peaks at $\sim$ 150 and $\sim$ 197 cm^{-1} as E_{1g} and E_{2g} modes arising from the folding of La M^{3+} and M^{2+} modes of the $P6_3/mmc$ phase, respectively.

Space group	Lattice parameters	Wyckoff positions		
$Fm\bar{3}m$	$a = 5.13709$ Å	La **4b**	$[\frac{1}{2}, \frac{1}{2}, \frac{1}{2}]$	
		H **8c**	$[\frac{1}{4}, \frac{1}{4}, \frac{1}{4}]$	
	Volume/f.u. = 33.89 Å^3	H **32f**	$[x_f, x_f, x_f]$	$x_f = 0.87908$
$P6_3/mmc$	$a = 3.72120$ Å	La **2c**	$[\frac{1}{3}, \frac{2}{3}, \frac{1}{4}]$	
	$c = 5.68038$ Å	H **4e**	$[0, 0, z_e]$	$z_e = 0.35384$
		H **4f**	$[\frac{1}{3}, \frac{2}{3}, z_f]$	$z_f = 0.61510$
	Volume/f.u. = 34.06 Å^3	H **12k**	$[x_k, 2x_k, z_k]$	$x_k = 0.83410$, $z_k = 0.08601$
$P6_3/m$	$a = 7.45130$ Å	La **2c**	$[\frac{1}{3}, \frac{2}{3}, \frac{1}{4}]$	
	$c = 5.67802$ Å	La **6h**	$[x_h, y_h, \frac{1}{4}]$	$x_h = 0.83259$, $y_h = 0.16563$
		H **4e**	$[0, 0, z_e]$	$z_e = 0.34603$
		H **4f**	$[\frac{1}{3}, \frac{2}{3}, z_f]$	$z_f = 0.61619$
		H **12i**	$[0.16664, 0.08117, 0.91759]$	
		H **12i**	$[0.16724, 0.58398, 0.91395]$	
		H **12i**	$[0.67170, 0.08756, 0.91236]$	
		H **12i**	$[0.65834, 0.57907, 0.91780]$	
		H **12i**	$[0.99935, 0.49028, 0.64746]$	
	Volume/f.u. = 34.13 Å^3	H **12i**	$[0.33147, 0.17916, 0.88389]$	

Supplementary Table 1: **Computed structural parameters** Structural parameters of fcc, hpc and distorted hpc phases evaluated from DFT calculations at a classical pressure of 135 GPa. Wyckoff positions are given in crystal coordinates and only for a representative site for each Wyckoff orbit, as the other positions can be obtained by applying the corresponding space-group symmetry operations.

$P6_3/mmc$ (# 194)								$P6_3/m$ (# 176)			
Γ (D_{6h})				M (D_{2h})				Γ (C_{6h})			
		Static	Dynamic			Static				Static	Dynamic
Γ_5^+	(E_{2g})	89.5 [83.3]	125.8 [120.7]					$\Gamma_3^+ \oplus \Gamma_5^+$	(E_{2g})	102.2 [90.3]	154.4 [144.8]
				M_3^+	(B_{2g})	139.8 [135.4]		$\Gamma_4^+ \oplus \Gamma_6^+$	(E_{1g})	150.6 [131.9]	163.6 [159.8]
								Γ_2^+	(B_g)	178.0 [172.9]	179.6 [173.9]
				M_1^+	(A_g)	142.7 [134.2]		$\Gamma_3^+ \oplus \Gamma_5^+$	(E_{2g})	164.6 [160.4]	182.4 [178.4]
								Γ_1^+	(A_g)	178.1 [176.8]	179.0 [177.8]
				M_2^+	(B_{1g})	182.6 [181.3]		Γ_1^+	(A_g)	185.1 [180.9]	192.8 [189.5]
								$\Gamma_3^+ \oplus \Gamma_5^+$	(E_{2g})	197.0 [192.5]	210.9 [198.3]
Γ_4^+	(B_{1g})	254.1 [253.3]	256.1 [255.4]								

Supplementary Table 2: **Calculated phonon frequencies in the static harmonic approximation.** La-derived phonon modes that can display Raman optical activity. Phonon modes are labeled according to the irreducible representations of the point group relevant for the crystal structure and phonon momentum, using the Miller-Love notation (Mulliken notation in round brackets). Phonon (static) frequencies are given in cm^{-1} in the limit of infinitely small Hydrogen mass, the corresponding value obtained for the physical m_H being given in square brackets. For the higher-symmetry hpc-LaH_{10} phase we list the two La phonons at Γ, only one of which is Raman active; the optically inactive phonon is written in gray. We further provide the phonon frequencies of inversion-even modes at the M point whose folding in the lower-symmetric $2\times2\times1$ reconstruction gives rise to additional Raman-active phonon modes. The folding of the M_3^+ mode in the zone center of the $P6_3/m$ produces a Raman-active E_{1g} mode and an optical inactive B_g mode (gray-shaded) that appears to hybridize with the zone-center phonon mode labeled as Γ_4^+ in the high-symmetry structure. **Extended Data Table 1** compares the ab initio frequencies of the $P6_3/m$ reconstruction with the values obtained from the analysis of the experimental spectra.

.

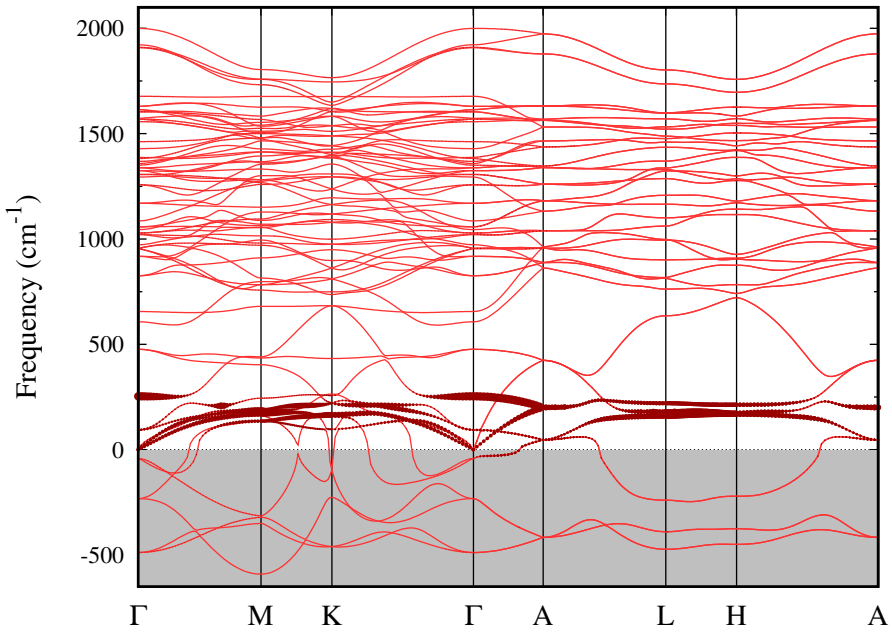

Supplementary Figure 1: **Phonon dispersion of hpc-LaH$_{10}$ from DFT.** Harmonic phonon dispersion of hexagonal LaH$_{10}$ in the $P6_3/mmc$ phase, interpolated from a 2×2×2 grid comprinsing the high-symmetry points Γ, A, L and M. The phonon modes with dominant La character in the frequency range 0-250 cm^{-1} is highlighted by dark-red points whose size is proportional to the La contribution. The grey shading marks the region with unstable (imaginary) phonon frequencies, here depicted as negative frequencies. The strongest dynamical instability occurs for a B_{1g} (M_2^+ in Miller-Love notation) phonon mode contributed only by Hydrogens at the M point.

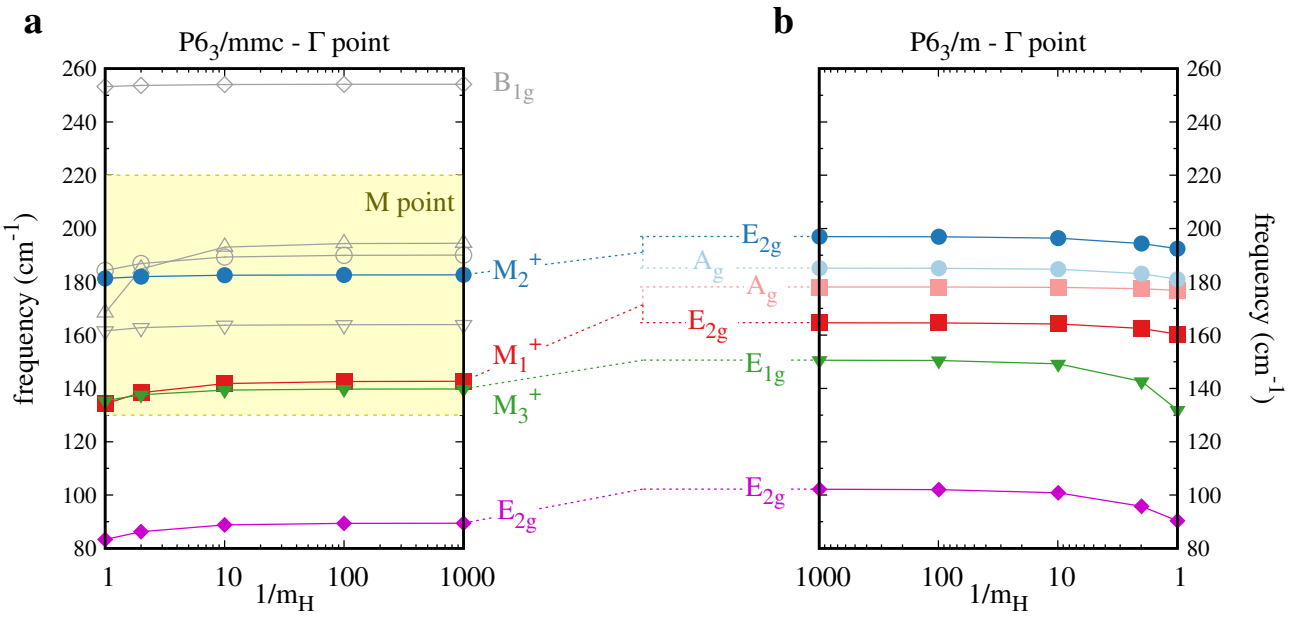

Supplementary Figure 2: **Lanthanum-derived Raman-active modes in ideal hpc-LaH$_{10}$ and in reconstructed cell.** In order to identify the interplay of La and H contribution in low-energy phonon modes with dominant Lanthanum character, we show the evolution of phonon frequencies as a function of inverse Hydrogen mass, where the Hydrogen contributions can be fully suppressed in the limit of vanishing m_H. **a** At Γ point of hpc-LaH$_{10}$ only two modes are significantly contributed by La atoms, a Raman-active E_{2g} and an optically inactive B_{1g} mode, displayed as grey empty symbols. Phonons are labeled using the Mulliken notation for the irreducible representations of the D_{6h} point group describing the symmetry properties at the Γ point. The coloured region highlights six La-derived phonon modes found at M point of LaH$_{10}$ in the $P6_3/mmc$ phase, labeled using the Miller-love notation. Among these only three are even under inversion and expected to give rise to Raman-active folded phonons. They are displayed with solid symbols with red, blue and green colours, while the inversion-odd partners are shown as empty grey symbols. Using Mulliken notation for the M point with D_{2h} point-group symmetries, the inversion-even modes correspond respectively to A_g, B_{1g} and B_{2g} irreducible representations. **b** Raman-active La-derived phonon modes for the 2×2×1 reconstructed cell with $P6_3/m$ symmetry (crystallographic point grop C_{6h}). The lowest E_{2g} mode corresponds to the zone-center Raman-active mode of the higher-symmetry $P6_3/mmc$ phase, that is however blue-shifted at slightly higher frequencies most probably as a consequence of the different H-sublattice. The folding of M_1^+ and M_2^+ phonons of the higher-symmetry structure split into $E_{2g} + A_g$ modes at the Γ point of the lower-symmetry phase, with a splitting of approximatively 12-14 cm^{-1}. Finally, M_3^+ phonons are zone-folded and split in a Raman-active E_{1g} mode (green solid triangles) strongly sensitive to the H-sublattice, and in a silent B_g mode (not shown) that is blue-shifted by $\sim$ 30 cm^{-1}.

Convention	"ladder" operator ϕ_μ	"displacement" operator $u_{s\alpha}$
Phonon propagator	$\tilde{D}_{\mu\nu}(t-t') = -i\left\langle \hat{T}\phi_\mu(t)\phi^\dagger_\nu(t')\right\rangle$	$D_{\mu\nu}(t-t') = -i\sqrt{M_s M_{s'}}\left\langle \hat{T}u_{s\alpha}(t)u^\dagger_{s'\beta}(t')\right\rangle \xi_{s\alpha,\mu}\xi_{s'\beta,\nu}$
Bare Phonon propagator	$\tilde{D}^{(0)}_{\mu\mu}(z) = \frac{2\omega^0_\mu}{z^2-(\omega^0_\mu)^2}$	$D^{(0)}_{\mu\mu}(z) = \frac{1}{z^2-(\omega^{\rm dyn}_\mu)^2}$
Dyson Equation	$\tilde{D}_{\mu\mu}(z) = 2\omega^0_\mu\left[z^2-(\omega^0_\mu)^2-2\omega^0_\mu\tilde{\Sigma}_\mu(z)\right]^{-1}$	$D_{\mu\mu}(z) = \left[z^2-(\omega^{\rm dyn}_\mu)^2-\Sigma_\mu(z)\right]^{-1}$
Phonon self energy	$\tilde{\Sigma}_\mu(z) = -\hbar 2N_{\rm F}\left\langle\lvert g_\mu\rvert^2\right\rangle_{S_F} I(z)$	$\Sigma_\mu(z) = (\omega^{\rm stat}_\mu-\omega^{\rm dyn}_\mu)^2 I(z)$
Phonon spectral func.	$\tilde{A}_\mu(\omega) = \lim_{z\to\omega+i0^+}{\rm Im}\,\frac{-2}{\pi}\tilde{D}_{\mu\mu}(z)$	$A_\mu(\omega) = \lim_{z\to\omega+i0^+}{\rm Im}\,\frac{-2z}{\pi}D_{\mu\mu}(z)$
Phonon spectral func. norm	$\int_{-\infty}^{\infty}\tilde{A}_\mu(\omega) = 0$	$\int_{-\infty}^{\infty}A_\mu(\omega) = 2$
Raman profile	$\tilde{\mathcal{P}}_\mu(\omega) = \frac{1}{4\omega^0_\mu}\tilde{A}_\mu(\omega)$	$\mathcal{P}_\mu(\omega) = \frac{1}{2\omega}A_\mu(\omega)$
Parameters	$\left\{\omega^0_\mu\,;\,-2N_{\rm F}\left\langle\lvert g_\mu\rvert^2\right\rangle_{S_F}\,;\,\eta_{imp}\right\}$	$\{\omega^{\rm dyn}_\mu\,;\,\omega^{\rm stat}_\mu\,;\,\eta_{imp}\}$

Supplementary Table 3: Definition of pivotal quantities in the "Dressed bubble" approximation for phonon propagator according to different conventions.

II Ab initio dressed bubble approximation for phonon spectral function

A Ladder operators convention

The central quantity in the many-body description of crystal vibrations is the phonon propagator $D_{\mu\nu}(z)$ defined as the retarded correlation of the phonon field operator ϕ_μ [Mahan 2000, p. 118]

$$\tilde{D}_{\mu\nu}(t-t') = -i\theta(t-t')\left\langle\phi_\mu(t)\phi^\dagger_\nu(t')\right\rangle, \tag{S1}$$

where $\theta(t)$ is the Heaviside function.

In order to describe the low-energy interaction between the electronic and ionic degrees of freedom, the electron-phonon coupling $g_{\mathbf{k}lm,\mathbf{q}\mu}$, relating two electronic states $|\mathbf{k}l\rangle$ and $|\mathbf{k}+\mathbf{q}m\rangle$ and a phonon mode μ, is introduced. Furthermore, in many cases, it is reasonable to neglect isolated degeneracy of the Fermi surface and thus it is reasonable to identify the Fermi contribution with the electronic intraband ($l=m$) excitation and higher-energy contributions with interband ($l\neq m$) transitions. In second quantization lattice vibrations are described by the creation (annihilation) operators $a^\dagger_{\mathbf{q}\mu}$ ($a_{\mathbf{q}\mu}$), so that the phonon field operators are $\phi_{\mathbf{q}\mu}(t) = \left(a_{\mathbf{q}\mu}e^{i\omega_{\mathbf{q}\mu}t}+a^\dagger_{\mathbf{q}\mu}e^{-i\omega_{\mathbf{q}\mu}t}\right)$. The physical displacement $u^L_{s\alpha}(t)$ of the s-th ion in the L unit-cell, along the α direction can be retrieved as [Mahan 2000, p. 10 eq. 1.85]

$$u^L_{s\alpha}(t) = \sum_{\mathbf{q}}\frac{e^{i\mathbf{q}\cdot\mathbf{R}_L}}{\sqrt{N}}u^{\mathbf{q}}_{s\alpha}(t) = \sum_{\mathbf{q}\mu}\frac{e^{i\mathbf{q}\cdot\mathbf{R}_L}}{\sqrt{N}}\sqrt{\frac{\hbar}{M_s 2\omega^0_{\mathbf{q}\mu}}}\xi^{s\alpha}_{\mathbf{q},\mu}\phi_{\mathbf{q}\mu}(t), \tag{S2}$$

where N is the number of unit cells considered in the Born-Von Karman boundary conditions, $\xi^{s\alpha}_{\mathbf{q},\mu}$ is the eigenvector of the phonon mode μ at the $\mathbf{q}$ point and ionic mass M_s. The system is then described by the following low-energy Hamiltonian [Maksimov and Shulga 1996, Eq. (2)]:

$$H = \sum_{\mathbf{k}l}\varepsilon_{\mathbf{k}l}c^\dagger_{\mathbf{k}l}c_{\mathbf{k}l} + \sum_{\mathbf{q}\mu}\hbar\omega^0_{\mathbf{q}\mu}\left(a^\dagger_{\mathbf{q}\mu}a_{\mathbf{q}\mu}+\frac{1}{2}\right) + \sum_{\mathbf{k}l,\mathbf{q}\mu}\hbar g_{\mathbf{k}l,\mathbf{q}\mu}c^\dagger_{\mathbf{k}l}c_{\mathbf{k}l}(a_{\mathbf{q}\mu}+a^\dagger_{-\mathbf{q}\mu}) \tag{S3}$$

where electronic states of energy $\varepsilon_{\mathbf{k}l}$ are populated by $c^\dagger_{\mathbf{k}l}$ operators, with "l" labelling both the band index and the electronic spin for a lighter notation.

From now on we consider only the $q=0$ case, being interested in the spectroscopic response of the system. The first building block for an evaluable expression of the phonon propagator, is the "bare" phonon propagator defined as the correlation in the ground state at zero temperature $\langle\cdot\rangle_0$

$$\tilde{D}^{(0)}_{\mu\nu}(t-t') = -i\theta(t-t')\left\langle\phi_\mu(t)\phi^\dagger_\nu(t')\right\rangle_0. \tag{S4}$$

Since at zero temperature the Fermi surface does not contribute, the bare phonon propagator coincides with the insulator-like contribution and thus it is completely described by the bare phonon frequency

$$\tilde{D}^{(0)}_{\mu\mu}(z) = \frac{2\omega^0_\mu}{z^2-(\omega^0_\mu)^2} \tag{S5}$$

where we express the time-dependent correlation in the complex frequency space $z = \omega + i\eta$.

The complete phonon propagator Eq. (**S**1) includes the effects of intraband electron-phonon interaction accounted for by the phonon self-energy $\tilde{\Sigma}_{\mu\mu'}(\omega)$ as defined by the following Dyson equation [Mahan 2000, Eq. (2.123)]:

$$\tilde{D}_{\mu\nu}(z) = \frac{\tilde{D}^{(0)}_{\mu\nu}(z)}{1 - \tilde{D}^{(0)}_{\mu\nu}(z)\tilde{\Sigma}_{\mu\nu}(z)} = \frac{2\omega^0_\mu}{z^2 - (\omega^0_\mu)^2 - 2\omega^0_\mu\tilde{\Sigma}_{\mu\nu}(z)}. \tag{S6}$$

For the sake of simplicity, we neglect the mode mixing that due to $\tilde{\Sigma}_{\mu\nu}(z)$ and focus on just the diagonal terms. Besides being a valid approximation whenever the phonon frequencies are well-separated, this approximation can be easily lifted. Secondly, we assume that the contributions at the Fermi level are isotropic. Neglecting anisotropy greatly simplified the derivation since it allows reducing the 3D integral over momenta $\mathbf{k}$ to the energy integral over $|\mathbf{k}|$. Furthermore, it implies that all quantities computed at the Fermi level coincide with their average over the Fermi surface, starting from the electron-phonon coupling $g_{\mathbf{k}l,\mu}$ whose Fermi average is:

$$\left\langle |g_{\mathbf{k}l,\mu}|^2 \right\rangle_{S_F} = -\frac{1}{2N_\mathrm{F}}\frac{2}{N_\mathbf{k}}\sum_{\mathbf{k},l} f'(\varepsilon_{\mathbf{k}l})|g_{\mathbf{k}l\mu}|^2 \tag{S7}$$

where N_F stands for the electronic density of state per spin at Fermi. The validity of the isotropic approximation is system-specific and has to be verified. While it was considered commonly valid [Allen and Mitrović 1983, p. 45] [Shepelev 1969], the recent study [Lucrezi et al. 2024] questions its applicability to super-Hydrides. The agreement between the theoretical isotropic model and experimental observations supports the validity of the isotropic approximation in the case of h-LaH_{10}. The general anisotropic theory is discussed in [Allen and Mitrović 1983] and [Marchese et al. 2024], we leave the generalization of the present implementation to the anisotropic case to subsequent studies.

The isotropic phonon self-energy reads as in [Zeyher and Zwicknagl 1988, Eq. (13)] and [Maksimov and Shulga 1996, Eq. (13)]:

$$\tilde{\Sigma}_\mu(z) = -\hbar 2N_\mathrm{F}\left\langle |g_{\mathbf{k}l,\mu}|^2 \right\rangle_{S_F} I(z) \tag{S8}$$

where the dimensionless function $I(z)$ defined as [Zeyher and Zwicknagl 1988, Eq. (8)]:

$$I(z) = -\frac{k_\mathrm{B}T}{2N_\mathrm{F}N_k}\sum_{\mathbf{k}i,\Omega_n} \mathrm{Tr}\left[\hat{\tau}_3\hat{G}_{\mathbf{k}i}(i\Omega_n)\hat{\tau}_3\hat{G}_{\mathbf{k}i}(i\Omega_n + i\omega_m)\right]_{i\omega_m\Rightarrow z}, \tag{S9}$$

encodes completely the temperature and frequency dependence of the phonon self-energy. The electronic propagator appearing in (**S**9) is written in the Nambu spinor representation and accounts for the electron-phonon and impurity scattering and the Cooper pairs formation across the SC transition. Its explicit form is then found solving the Migdal-Eliashberg systems of equations for a given Eliashberg function $\alpha^2F(\omega)$ determining the electron-phonon coupling. Once the dimensionless function and thus the phonon propagator is found, the peak profile entering the vibrational Raman contribution can be written as:

$$\tilde{\mathcal{P}}^{vib}_\mu(\omega) = \frac{\tilde{A}_\mu(\omega)}{4\omega^0_\mu}, \tag{S10}$$

where the phonon spectral function is commonly defined as [Mahan 2000, Eq. (3.114)]

$$\tilde{A}_\mu(\omega) = -\lim_{z\to\omega+i0^+}\mathrm{Im}\,\frac{2}{\pi}\tilde{D}_{\mu\mu}(z), \tag{S11}$$

with the following normalization properties:

$$\int_{-\infty}^{\infty} d\omega\tilde{A}_\mu(\omega) = 0 \qquad \int_0^\infty d\omega\tilde{A}_\mu(\omega) = 2\omega^0_\mu. \tag{S12}$$

In conclusion, this many-body approach requires estimating only three parameters entering the (low-energy) effective model: the bare phonon frequency ω^0_μ, the electron-phonon coupling contribution of the Fermi surface $-2N_\mathrm{F}\left\langle |g_{\mathbf{k}l,\mu}|^2 \right\rangle_{S_F}$ and the level of impurities η_{imp}. An example of obtaining the electron-phonon coupling contribution from the experimental data can be found in [Cappelluti 2006], where the value of $-2N_\mathrm{F}\left\langle |g_{\mathbf{k}l,\mu}|^2 \right\rangle_{S_F}$ is estimated by the zero-point motion while ω^0_μ is treated as a fitting parameter of the model. In the following section, we rewrite these quantities in a slightly different convention required for expressing these phenomenological parameters in terms of ab initio quantities evaluable in DFT. **Supplementary Table 3** reports the main quantities for the "dressed bubble" approximation in the two conventions.

B The displacement operator convention

To draw a connection between the many-body formalism and the ab initio framework based on DFPT, it is convenient to adopt a different definition of the phonon propagator based on displacement operators $u_{s\alpha}$ rather than field operators A_μ[Abrikosov et al. 1975]:

$$D_{ss'\alpha\beta}(t-t') = -i\sqrt{M_s M_{s'}}\theta(t-t')\left\langle u_{s\alpha}(t)u^\dagger_{s'\beta}(t')\right\rangle. \tag{S13}$$

The equivalence of the two conventions is insured by the linearity of Eq. (S2) relating field and displacement operator. Choosing the displacement operator as the descriptor of the lattice vibrations implies that the coupling between the electronic and the ionic degrees of freedom should be replaced accordingly. Thus, the "electron-displacement" coupling $V_{\mathbf{k}l,\mathbf{q}s\alpha}$, also known as "deformation potential", assumes the role of the electron-phonon coupling $g_{\mathbf{k}l,\mu}$. If we write the deformation potential in the normal mode basis as:

$$V_{\mathbf{k}l,\mu} = \sum_{s\alpha}\sqrt{\frac{1}{\hbar M_s}}\xi_{\mu,s\alpha}V_{\mathbf{k}l,s\alpha}, \tag{S14}$$

we find that the two coupling are related by a linear relation [Giustino 2017]:

$$V_{\mathbf{k}l,\mu} = \sqrt{2\omega^0_\mu}g_{\mathbf{k}l,\mu}. \tag{S15}$$

Following the same steps of the previous section we find that the bare phonon propagator in this convention reads

$$D^{(0)}_\mu(z) = \xi_{\mu,s\alpha}\xi_{\mu,s'\beta}D^{(0)}_{ss'\alpha\beta}(z) = \frac{1}{z^2-(\omega^0_\mu)^2}; \tag{S16}$$

the complete phonon propagator is then

$$D_\mu(z) = \frac{1}{z^2-(\omega^0_\mu)^2-\Sigma_\mu(z)} \tag{S17}$$

and the self-energy at leading order is

$$\Sigma_\mu(z) = -2N_{\mathrm{F}}\hbar\left\langle|V_{\mathbf{k}l\mu}|^2\right\rangle_{S_F} I(z). \tag{S18}$$

The spectral function in this convention has the following definition for the phonon spectral function (as [Berges et al. 2023] equivalent to [Abrikosov et al. 1975, Eq. (7.29)])

$$A_\mu(\omega) = -\lim_{z\to\omega+i0^+}\mathrm{Im}\,\frac{2z}{\pi}D_\mu(z). \tag{S19}$$

and its normalization properties are independent of the bare phonon frequency

$$\int_{-\infty}^{\infty}d\omega A_\mu(\omega) = 2 \qquad \int_0^\infty d\omega A_\mu(\omega) = 1 \tag{S20}$$

as proved in Section C. Finally, the peak profile for the vibrational Raman contribution is:

$$\mathcal{P}^{vib}_\mu(\omega) = \frac{A_\mu(\omega)}{2\omega}. \tag{S21}$$

Wrapping up the comparison between these two conventions, we see how the linear relation between the two operators

$$\phi_\mu = \sqrt{\frac{M_s 2\omega^0_\mu}{\hbar}}\xi_{\mu,s\alpha}u_{s\alpha} \tag{S22a}$$

propagates to the following quantities:

$$\left\langle|V_{\mathbf{k}l,\mu}|^2\right\rangle_{S_F} = 2\omega^0_\mu\left\langle|g_{\mathbf{k}l,\mu}|^2\right\rangle_{S_F} \tag{S22b}$$

$$\Sigma_\mu(z) = 2\omega^0_\mu\tilde{\Sigma}_\mu(z) \tag{S22c}$$

$$D_\mu(z) = \frac{1}{2\omega^0_\mu}\tilde{D}_\mu(z) \tag{S22d}$$

$$A_\mu(\omega) = \frac{\omega}{2\omega^0_\mu}\tilde{A}_\mu(\omega) \tag{S22e}$$

$$\mathcal{P}_\mu(\omega) = \frac{2\omega^0_\mu}{\omega}\tilde{\mathcal{P}}_\mu(\omega). \tag{S22f}$$

As a consequence of this mapping, the parameters to be calculated in this convention are $\left\langle |V_{\mathbf{k}l,\mu}|^2 \right\rangle_{S_F}$ quantifying the electron-phonon coupling of the Fermi surface; and ω_μ^0 describing the insulator-like contribution that does not include the Fermi surface contribution. As detailed in the method section, the following identities allows to easily calculated these parameters in a DFPT framework:

$$-\hbar 2 N_{\mathrm{F}} \left\langle |V_{\mathbf{k}l\mu}|^2 \right\rangle_{S_F} = (\omega_\mu^{\mathrm{stat}})^2 - (\omega_\mu^{\mathrm{dyn}})^2 \tag{S23}$$

$$\omega_\mu^0 = \omega_\mu^{\mathrm{dyn}}. \tag{S24}$$

C Spectral function

A similar arbitrariness is present in the definition of the phonon spectral function. We find useful the following definition for the phonon spectral function due to its normalization properties (S19).

The reasons for adopting this phonon spectral function definition are to be found in the following proof of the normalization properties of Eq. (S19) follows. We can calculate the norm of the spectral function solving the following integral

$$\int_{-\infty}^{\infty} d\omega A_\mu(\omega + i0^+) = \frac{-2}{\pi} \operatorname{Im} \int_{-\infty}^{\infty} d\omega \frac{\omega + i0^+}{(\omega + i0^+)^2 - (\omega_\mu^{\mathrm{dyn}})^2 - \Sigma_\mu(\omega + i0^+)} \tag{S25}$$

in the complex space taking advantage of the of the analytic properties of the phonon self-energy. Since the imaginary part of the phonon self-energy is an odd function of the frequency and has negative values for positive frequencies, the $A_\mu(z)$ has only poles in the lower half of the complex space.

Then, the normalization integral can be calculated considering a closed line-integral in the upper half-plane consisting in a $2R$ length segment of the real axis and an half-circumference of radius R. Since there are no poles enclosed in such simple closed curve, the total integral is null thanks to the Cauchy theorem. As a consequence, the integral over the real axis is equal to minus the half-circumference contribution in the limit of infinite radius R. We proceed calculating the half-circumference contribution:

$$\frac{-2}{\pi} \operatorname{Im} \lim_{R\to\infty} \int_0^{\pi} d\theta (iRe^{i\theta}) \frac{Re^{i\theta}}{(Re^{i\theta})^2 - (\omega_\mu^{\mathrm{dyn}})^2 - \Sigma_\mu(Re^{i\theta})}. \tag{S26}$$

Assuming that asymptotically the self-energy becomes a constant due to the absence of high energy interaction, we can simplify the denominator in the asymptotic regime defining the complex constant $\mathcal{Z} = (\omega_\mu^{\mathrm{dyn}})^2 + \Sigma_\mu(Re^{i\theta})$ for $R \gg R_c$ and thus:

$$\int_{-\infty}^{\infty} d\omega A_\mu(\omega + i0^+) = \frac{2}{\pi} \operatorname{Im} \lim_{R\to\infty} \int_0^{\pi} d\theta \frac{i(Re^{i\theta})^2}{(Re^{i\theta})^2 - \mathcal{Z}} = \frac{2}{\pi} \operatorname{Im} \int_0^{\pi} d\theta \left[\lim_{R\to\infty} \frac{i}{1 - \frac{\mathcal{Z}}{(Re^{i\theta})^2}} \right] = \frac{2}{\pi} \operatorname{Im} \int_0^{\pi} d\theta i = 2. \tag{S27}$$

III Pressure estimation from Raman spectrum

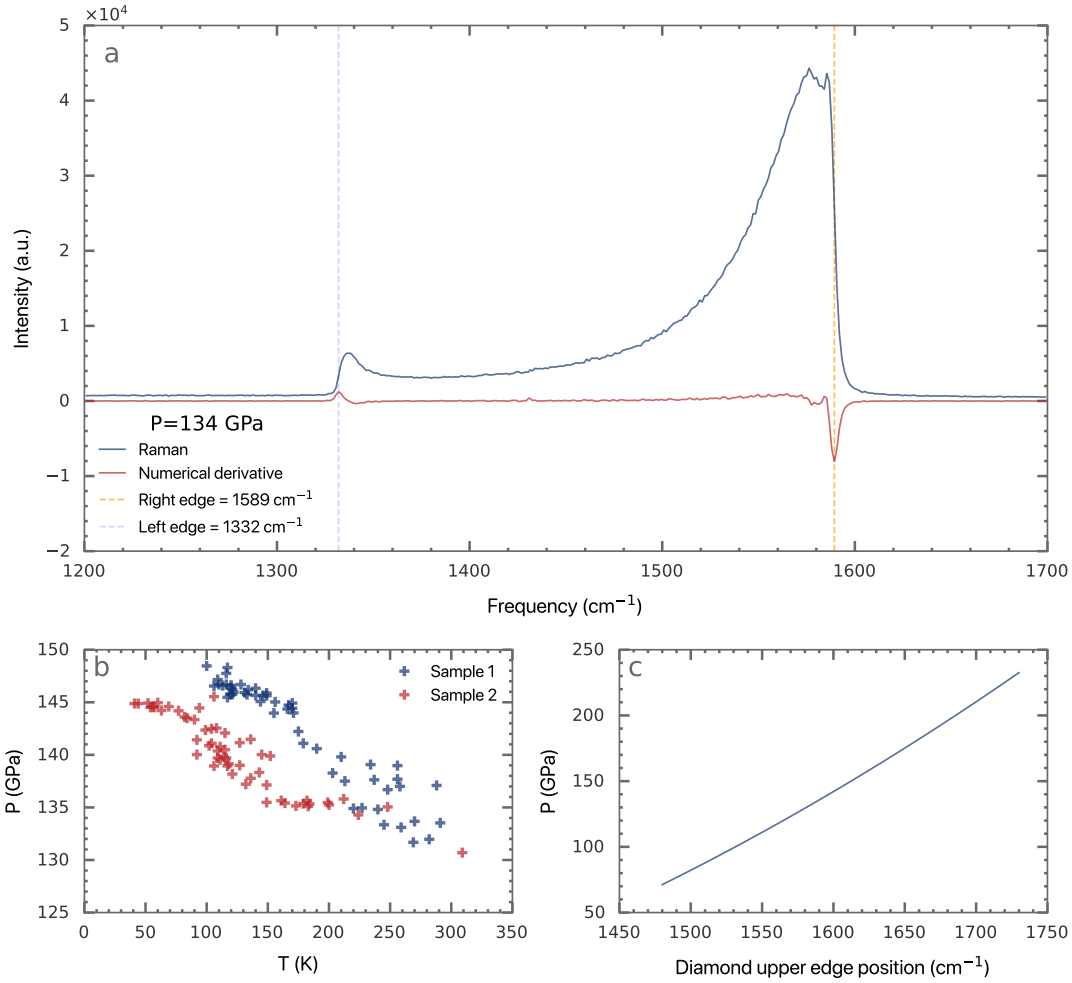

Supplementary Figure 3: **Pressure determination from the stressed diamond Raman phonon. Panel a** shows the Raman from the stressed diamond (blue curve) and its derivative (red curve). The maxima and the minima in the derivative mark the unstressed and stressed edges of the diamond signal, respectively. The two edges are marked by vertical dashed lines and are then used to determine the pressure Akahama and Kawamura 2006. As shown in **panel b**, our datasets demonstrate an increase in pressure when decreasing temperature, typical for high-pressure studies.

References

Laniel, Dominique et al. (Nov. 2022). "High-pressure synthesis of seven lanthanum hydrides with a significant variability of hydrogen content". en. In: *Nature Communications* 13.1, p. 6987. ISSN: 2041-1723. DOI: 10.1038/s41467-022-34755-y. URL: https://www.nature.com/articles/s41467-022-34755-y (cit. on p. 1).

Peng, Feng et al. (Sept. 2017). "Hydrogen Clathrate Structures in Rare Earth Hydrides at High Pressures: Possible Route to Room-Temperature Superconductivity". In: *Physical Review Letters* 119.10, p. 107001. DOI: 10.1103/PhysRevLett.119.107001. URL: https://link.aps.org/doi/10.1103/PhysRevLett.119.107001 (cit. on p. 1).

Shipley, Alice M. et al. (June 2020). "Stability and superconductivity of lanthanum and yttrium decahydrides". In: *Physical Review B* 101.22, p. 224511. DOI: 10.1103/PhysRevB.101.224511. URL: https://link.aps.org/doi/10.1103/PhysRevB.101.224511 (cit. on pp. 1, 2).

Errea, Ion, Francesco Belli, et al. (Feb. 2020). "Quantum Crystal Structure in the 250-Kelvin Superconducting Lanthanum Hydride". In: *Nature* 578.7793, pp. 66–69. ISSN: 1476-4687. DOI: 10.1038/s41586-020-1955-z. URL: http://www.nature.com/articles/s41586-020-1955-z (cit. on pp. 1, 2).

Drozdov, A. P. et al. (May 2019). "Superconductivity at 250 K in lanthanum hydride under high pressures". en. In: *Nature* 569.7757, pp. 528–531. ISSN: 1476-4687. DOI: 10.1038/s41586-019-1201-8. URL: https://www.nature.com/articles/s41586-019-1201-8 (cit. on p. 1).

Liu, Hanyu et al. (Sept. 2018). "Dynamics and superconductivity in compressed lanthanum superhydride". In: *Physical Review B* 98.10, p. 100102. DOI: 10.1103/PhysRevB.98.100102. URL: https://link.aps.org/doi/10.1103/PhysRevB.98.100102 (cit. on p. 1).

Sun, Dan et al. (Nov. 2021). "High-Temperature Superconductivity on the Verge of a Structural Instability in Lanthanum Superhydride". In: *Nature Communications* 12.1, p. 6863. ISSN: 2041-1723. DOI: 10.1038/s41467-021-26706-w. URL: http://www.nature.com/articles/s41467-021-26706-w (cit. on p. 1).

Eremets, M. I. et al. (Apr. 2022). "High-Temperature Superconductivity in Hydrides: Experimental Evidence and Details". en. In: *Journal of Superconductivity and Novel Magnetism* 35.4, pp. 965–977. ISSN: 1557-1947. DOI: 10.1007/s10948-022-06148-1. URL: https://doi.org/10.1007/s10948-022-06148-1 (cit. on p. 1).

Perdew, John P., Kieron Burke, and Matthias Ernzerhof (Oct. 1996). "Generalized Gradient Approximation Made Simple". In: *Phys. Rev. Lett.* 77 (18), pp. 3865–3868. DOI: 10.1103/PhysRevLett.77.3865. URL: https://link.aps.org/doi/10.1103/PhysRevLett.77.3865 (cit. on p. 1).

Baroni, Stefano et al. (July 2001). "Phonons and related crystal properties from density-functional perturbation theory". In: *Rev. Mod. Phys.* 73 (2), pp. 515–562. DOI: 10.1103/RevModPhys.73.515. URL: https://link.aps.org/doi/10.1103/RevModPhys.73.515 (cit. on p. 2).

Giannozzi, Paolo et al. (Sept. 2009). "QUANTUM ESPRESSO: a modular and open-source software project for quantum simulations of materials". In: *Journal of Physics: Condensed Matter* 21.39, p. 395502. DOI: 10.1088/0953-8984/21/39/395502. URL: https://dx.doi.org/10.1088/0953-8984/21/39/395502 (cit. on p. 2).

Giannozzi, P et al. (Oct. 2017). "Advanced capabilities for materials modelling with Quantum ESPRESSO". In: *Journal of Physics: Condensed Matter* 29.46, p. 465901. DOI: 10.1088/1361-648X/aa8f79. URL: https://dx.doi.org/10.1088/1361-648X/aa8f79 (cit. on p. 2).

Hamann, D. R. (2013). "Optimized norm-conserving Vanderbilt pseudopotentials". In: *Phys. Rev. B* 88, p. 085117 (cit. on p. 2).

van Setten, M.J. et al. (2018). "The PseudoDojo: Training and grading a 85 element optimized norm-conserving pseudopotential table". In: *Comput. Phys. Commun.* 226, pp. 39–54. DOI: https://doi.org/10.1016/j.cpc.2018.01.012 (cit. on p. 2).

Errea, Ion, Matteo Calandra, et al. (Apr. 2016). "Quantum hydrogen-bond symmetrization in the superconducting hydrogen sulfide system". In: *Nature* 532.7597, pp. 81–84. ISSN: 1476-4687. DOI: 10.1038/nature17175. URL: http://www.nature.com/articles/nature17175 (cit. on p. 2).

Belli, Francesco and Ion Errea (Oct. 2022). "Impact of ionic quantum fluctuations on the thermodynamic stability and superconductivity of $LaBH_8$". In: *Phys. Rev. B* 106 (13), p. 134509. DOI: 10.1103/PhysRevB.106.134509. URL: https://link.aps.org/doi/10.1103/PhysRevB.106.134509 (cit. on p. 2).

Mahan, Gerald D. (2000). *Many-particle physics*. 3rd ed. Physics of solids and liquids. New York: Kluwer Academic/Plenum Publishers. ISBN: 978-0-306-46338-9 (cit. on pp. 6, 7).

Maksimov, E. G and S. V Shulga (Feb. 1996). "Nonadiabatic Effects in Optical Phonon Self-Energy". In: *Solid State Communications* 97.7, pp. 553–560. ISSN: 0038-1098. DOI: 10.1016/0038-1098(95)00745-8 (cit. on pp. 6, 7).

Allen, Philip B. and Božidar Mitrović (Jan. 1983). "Theory of Superconducting Tc". In: *Solid State Physics*. Ed. by Henry Ehrenreich, Frederick Seitz, and David Turnbull. Vol. 37. Academic Press, pp. 1–92. DOI: 10.1016/S0081-1947(08)60665-7 (cit. on p. 7).

Shepelev, A. G. (May 1969). "Gap Anisotropy in the Energy Spectrum of Superconductors". In: *Soviet Physics Uspekhi* 11.5, p. 690. ISSN: 0038-5670. DOI: 10.1070/PU1969v011n05ABEH003742. URL: https://iopscience.iop.org/article/10.1070/PU1969v011n05ABEH003742/meta (cit. on p. 7).

Lucrezi, Roman et al. (Jan. 2024). "Full-bandwidth anisotropic Migdal-Eliashberg theory and its application to superhydrides". en. In: *Communications Physics* 7.1, pp. 1–13. ISSN: 2399-3650. DOI: 10.1038/s42005-024-01528-6. URL: https://www.nature.com/articles/s42005-024-01528-6 (cit. on p. 7).

Marchese, Guglielmo et al. (Jan. 2024). "Born Effective Charges and Vibrational Spectra in Superconducting and Bad Conducting Metals". In: *Nature Physics* 20.1, pp. 88–94. ISSN: 1745-2481. DOI: 10.1038/s41567-023-02203-3 (cit. on p. 7).

Zeyher, R. and G. Zwicknagl (May 1988). "Phonon Self-Energy Effects Due to Superconductivity: Evidence for the Strong-Coupling Limit in $YBa_2Cu_3O_{7-\delta}$". In: *Solid State Communications* 66.6, pp. 617–622. ISSN: 0038-1098. DOI: 10.1016/0038-1098(88)90220-7. URL: https://www.sciencedirect.com/science/article/pii/0038109888902207 (cit. on p. 7).

Cappelluti, E. (Apr. 2006). "Electron-Phonon Effects on the Raman Spectrum in MgB_2". In: *Physical Review B* 73.14, p. 140505. DOI: 10.1103/PhysRevB.73.140505. URL: https://link.aps.org/doi/10.1103/PhysRevB.73.140505 (cit. on p. 7).

Abrikosov, Alekse Alekseevich, Lev Petrovich Gorkov, and I. E. Dzyaloshinski (Oct. 1975). *Methods of Quantum Field Theory in Statistical Physics*. Courier Corporation. ISBN: 978-0-486-63228-5 (cit. on p. 8).

Giustino, Feliciano (Feb. 2017). "Electron-Phonon Interactions from First Principles". In: *Reviews of Modern Physics* 89.1, p. 015003. DOI: 10.1103/RevModPhys.89.015003. URL: https://link.aps.org/doi/10.1103/RevModPhys.89.015003 (cit. on p. 8).

Berges, Jan et al. (Oct. 2023). "Phonon Self-Energy Corrections: To Screen, or Not to Screen". In: *Physical Review X* 13.4, p. 041009. DOI: 10.1103/PhysRevX.13.041009. URL: https://link.aps.org/doi/10.1103/PhysRevX.13.041009 (cit. on p. 8).

Akahama, Yuichi and Haruki Kawamura (Aug. 2006). "Pressure Calibration of Diamond Anvil Raman Gauge to 310GPa". In: *Journal of Applied Physics* 100.4, p. 043516. ISSN: 0021-8979. DOI: 10.1063/1.2335683. URL: https://doi.org/10.1063/1.2335683 (cit. on p. 10).

IV Spectra collection

In this section, we present the complete set of Raman spectra analysed, along with the results of the multi-peak fitting procedure. Not all fitted peaks were used to extract the parameters of the Migdal-Eliashberg model or plotted in the article figures. In the following collection of plots, the peaks included in the ME analysis are shown as shaded regions, while the unselected ones are displayed as hatched areas.

To ensure an unbiased selection of the data, we applied a filtering criterion based on the ratio ($r = \Delta x/|x|$) between the fitting uncertainty (Δx) and the fitted value (x) of each peak parameter –namely amplitude, position, and linewidth (c_i, ω_i, Γ_i in Eq. (2)). For sample 1, we excluded from the analysis all fits with ratios exceeding $r_A > 0.12$ for peak A, $r_D > 0.14$ for peak D, and $r_E > 0.30$ for peak E. An additional criterion was adopted for peak A, due to its sharpness, consisting in studying only spectra obtained with the 1200 gr/mm interferometer grating. For sample 2, we excluded results with $r_A > 0.28$, $r_D > 0.25$, and $r_E > 0.35$.

No threshold criterion was applied to peaks B and C, as their limited signal-to-noise ratio prevents a detailed Migdal-Eliashberg analysis. For these modes, only the averaged peak positions are reported in **Extended Data Table 1**.

Finally, we verified the robustness of our conclusions by testing multiple selection thresholds, finding no significant changes in the resulting analysis.

A Spectra sample 1

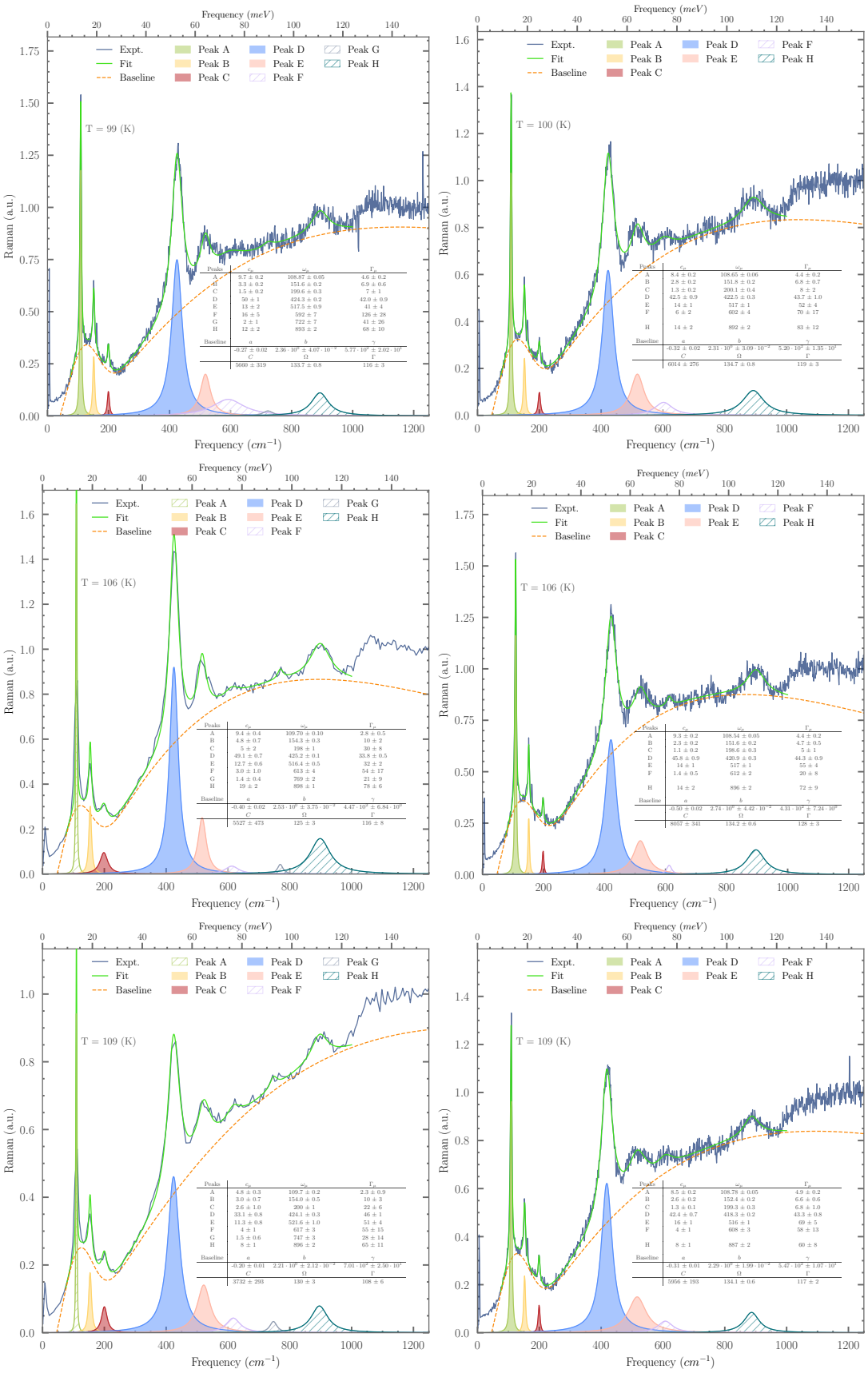
Frequency (meV)
Expt.
Fit
Baseline
Peak A
Peak B
Peak C
Peak D
Peak E
Peak F
Peak G
Peak H
T = 99 (K)
T = 100 (K)
T = 106 (K)
T = 106 (K)
T = 109 (K)
T = 109 (K)
Raman (a.u.)
Frequency (cm^{-1})

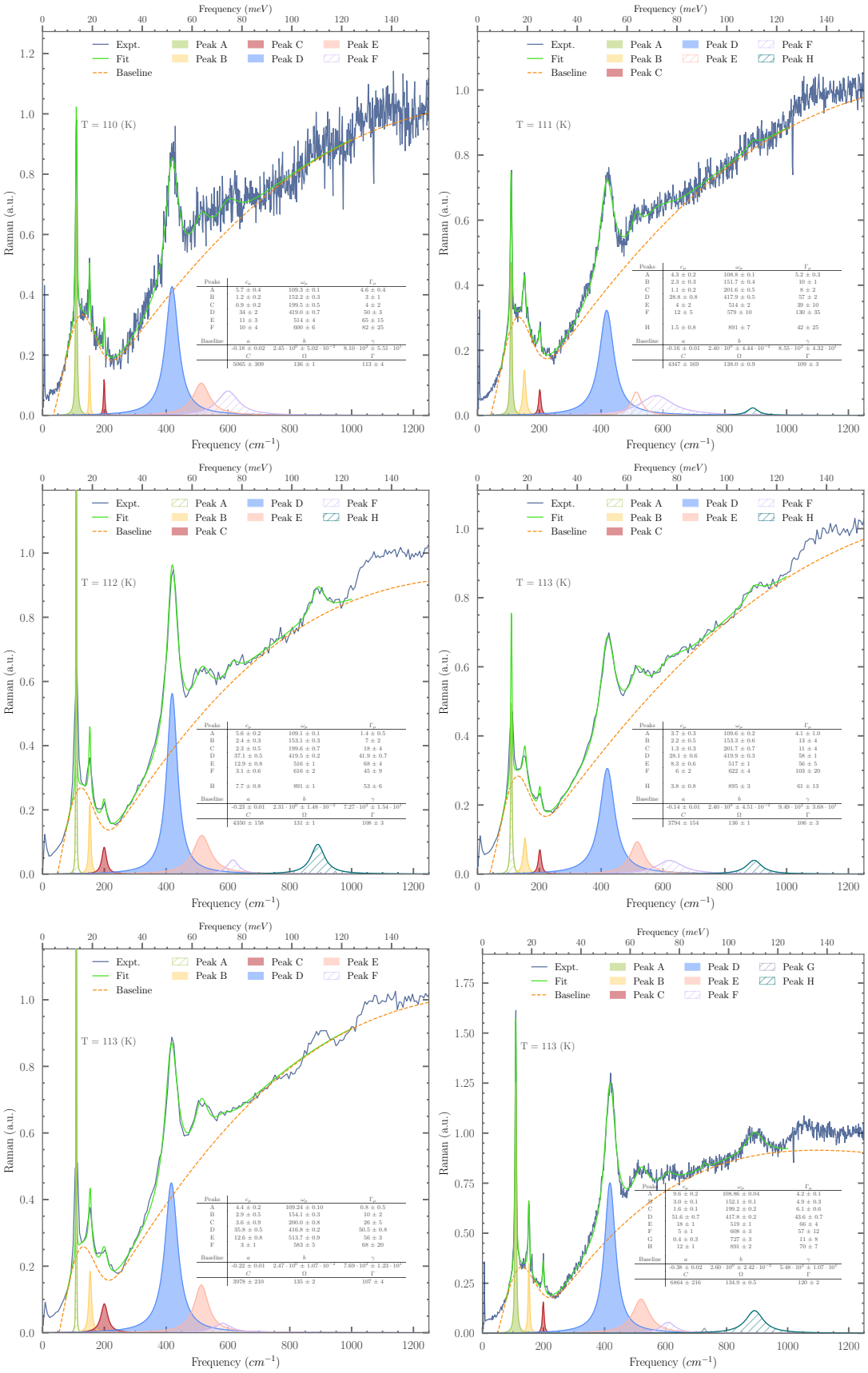
Frequency (meV)
Frequency (cm^{-1})
Raman (a.u.)
Expt.
Fit
Baseline
Peak A
Peak B
Peak C
Peak D
Peak E
Peak F
Peak G
Peak H
T = 110 (K)
T = 111 (K)
T = 112 (K)
T = 113 (K)
T = 113 (K)
T = 113 (K)

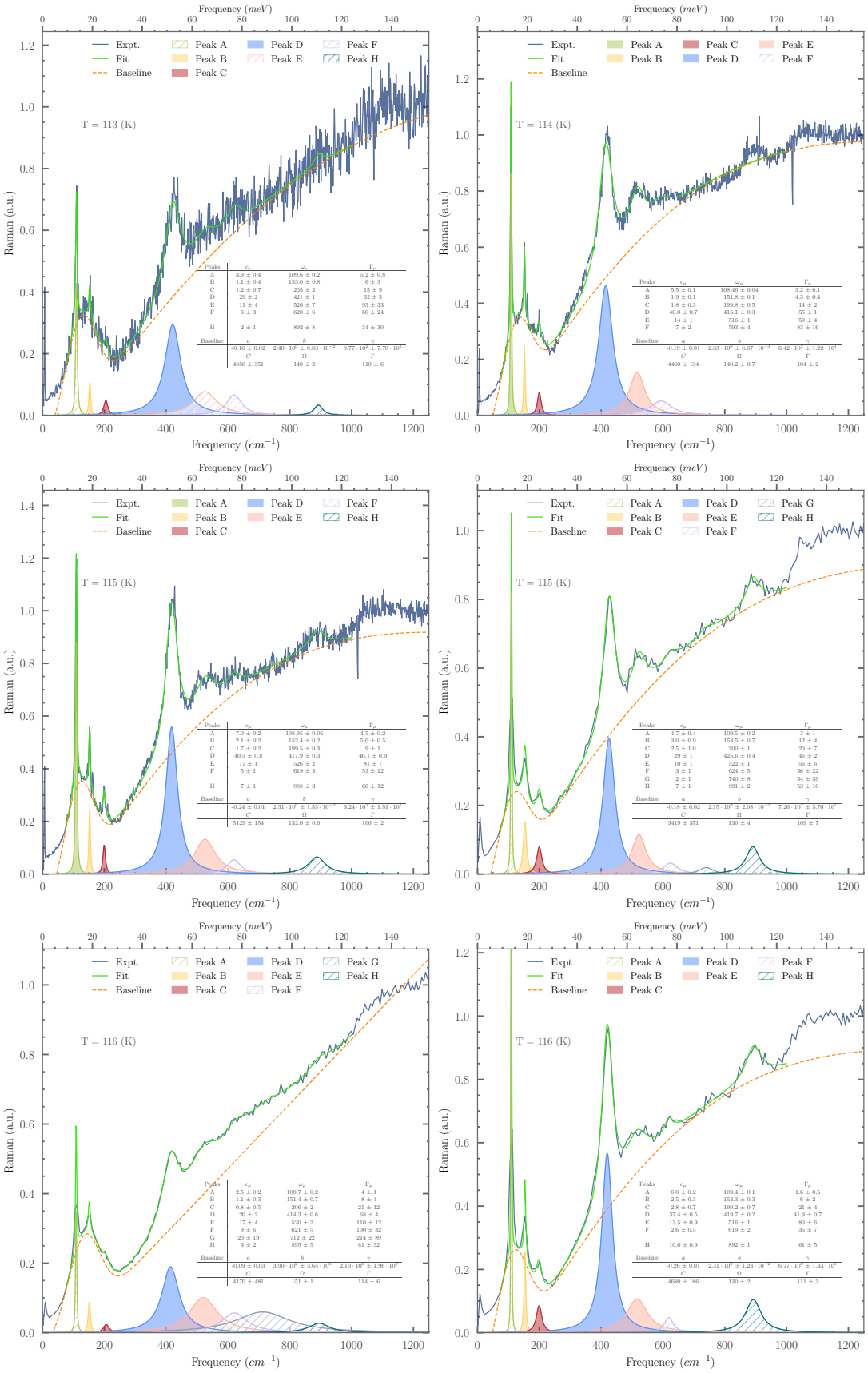
Frequency (meV)
Frequency (cm^{-1})
Raman (a.u.)
Expt.
Fit
Baseline
Peak A
Peak B
Peak C
Peak D
Peak E
Peak F
Peak G
Peak H
T = 113 (K)
T = 114 (K)
T = 115 (K)
T = 115 (K)
T = 116 (K)
T = 116 (K)

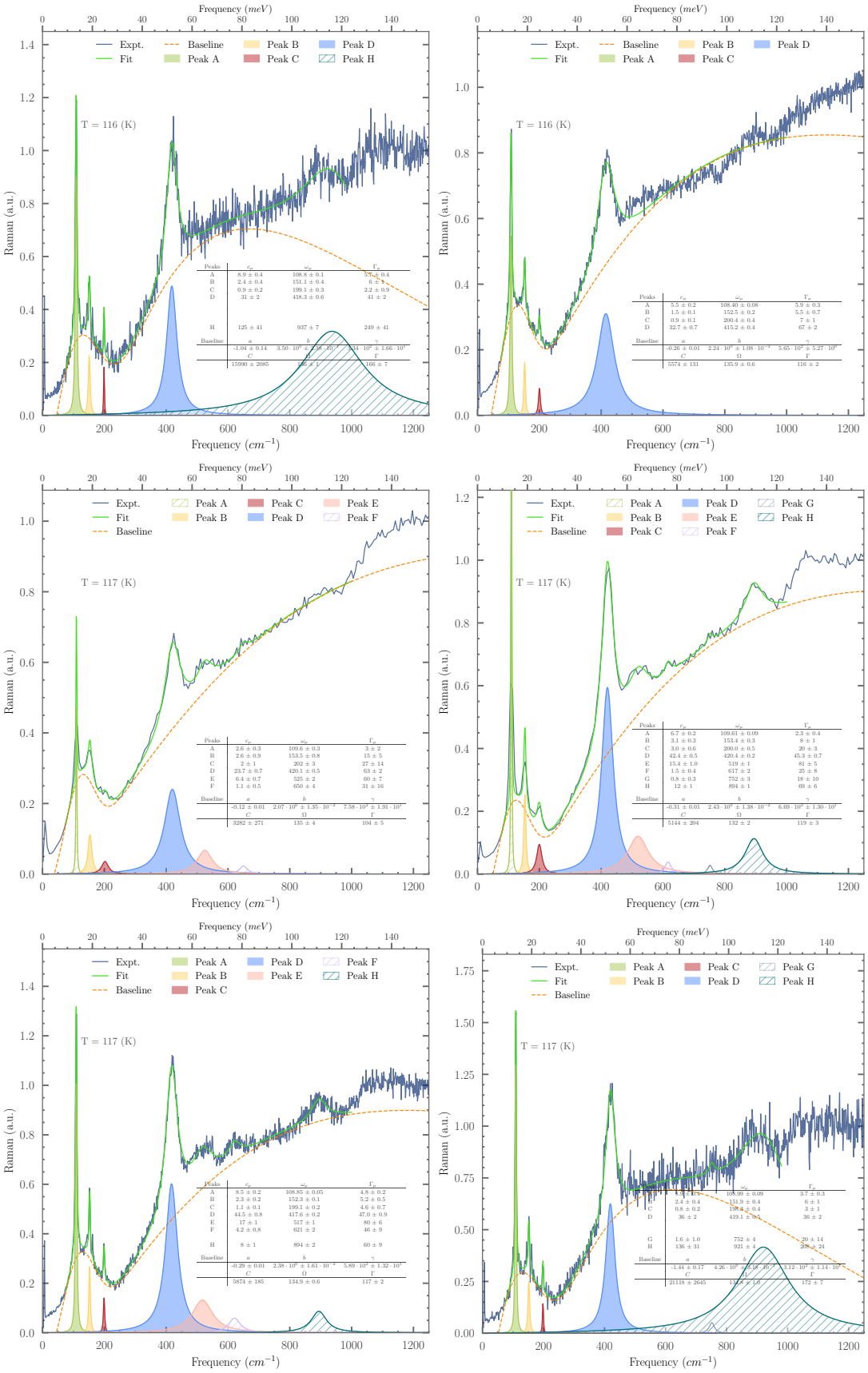
Frequency (meV)
Expt.
Fit
Baseline
Peak A
Peak B
Peak C
Peak D
Peak H
T = 116 (K)
Raman (a.u.)
Frequency (cm^{-1})
Peak A
Peak B
Peak C
Peak D
Peak E
Peak F
T = 117 (K)
Peak G
Peak H

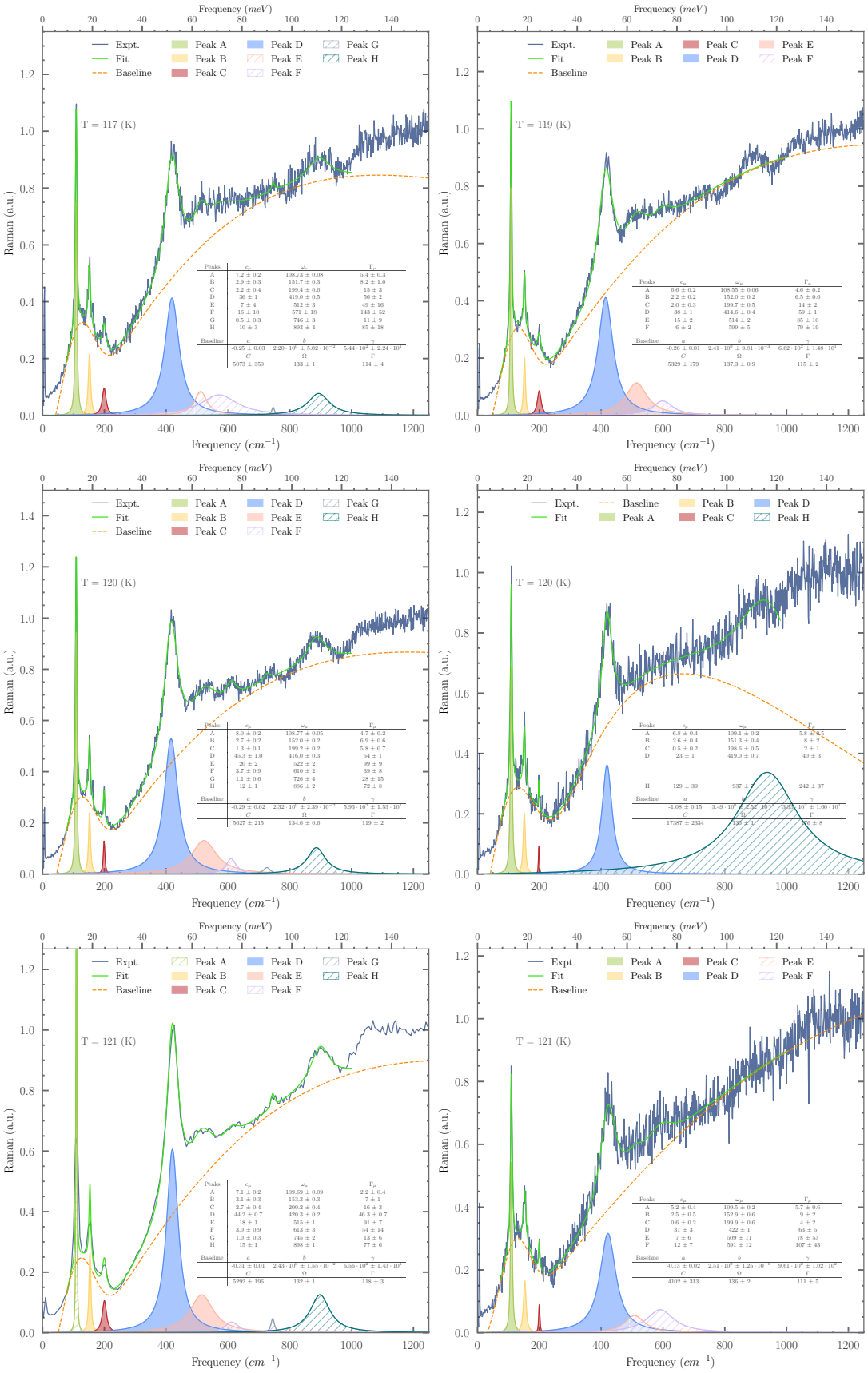
Frequency (meV)
Frequency (cm^{-1})
Raman (a.u.)
Expt.
Fit
Baseline
Peak A
Peak B
Peak C
Peak D
Peak E
Peak F
Peak G
Peak H
T = 117 (K)
T = 119 (K)
T = 120 (K)
T = 120 (K)
T = 121 (K)
T = 121 (K)

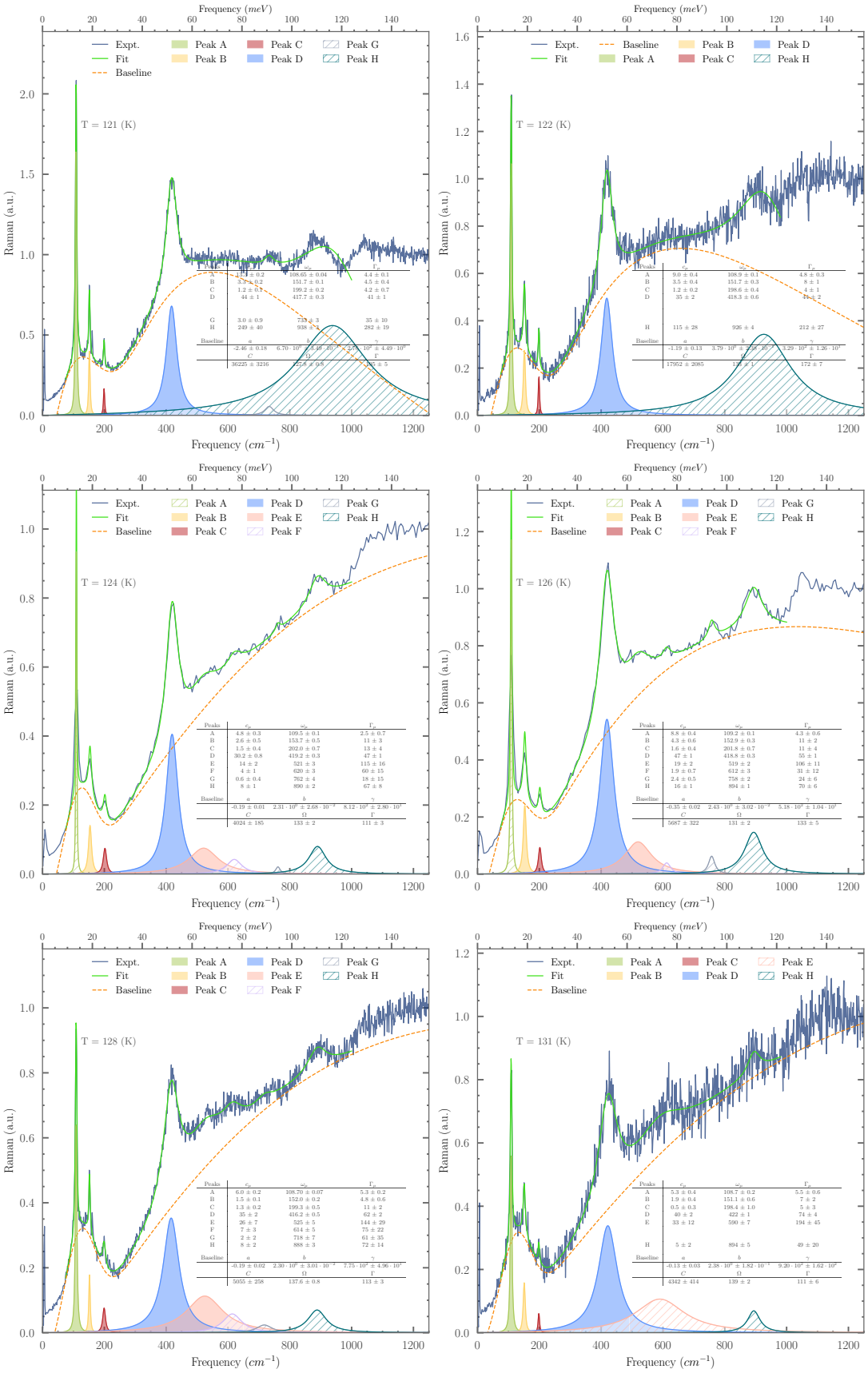
Frequency (meV)
Expt.
Fit
Baseline
Peak A
Peak B
Peak C
Peak D
Peak E
Peak F
Peak G
Peak H
T = 121 (K)
T = 122 (K)
T = 124 (K)
T = 126 (K)
T = 128 (K)
T = 131 (K)
Raman (a.u.)
Frequency (cm^{-1})

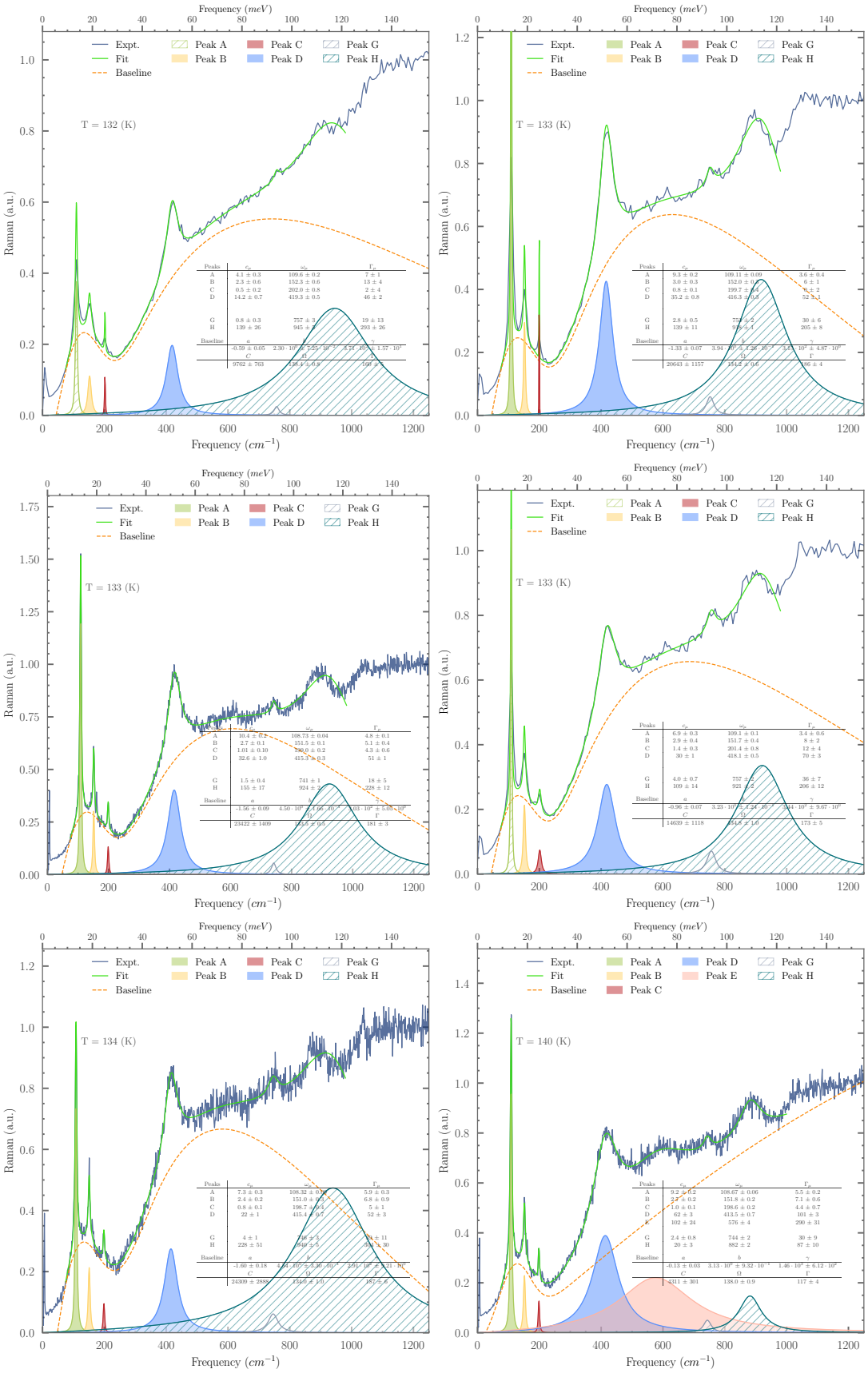
Frequency (meV)
Frequency (cm^{-1})
Raman (a.u.)
Expt.
Fit
Baseline
Peak A
Peak B
Peak C
Peak D
Peak E
Peak G
Peak H
T = 132 (K)
T = 133 (K)
T = 133 (K)
T = 133 (K)
T = 134 (K)
T = 140 (K)

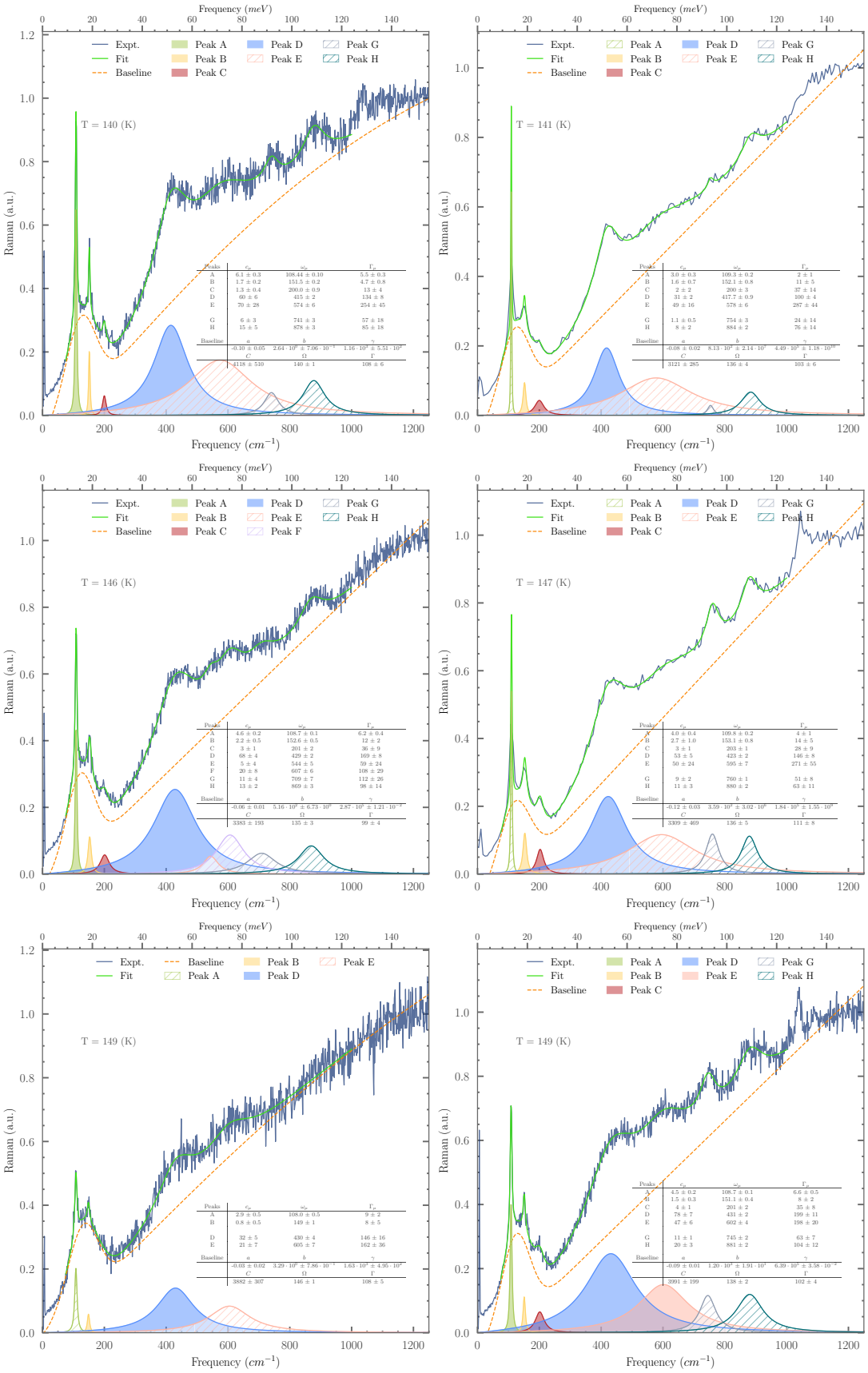
Frequency (meV)
Raman (a.u.)
Frequency (cm^{-1})
Expt.
Fit
Baseline
Peak A
Peak B
Peak C
Peak D
Peak E
Peak F
Peak G
Peak H
T = 140 (K)
T = 141 (K)
T = 146 (K)
T = 147 (K)
T = 149 (K)
T = 149 (K)

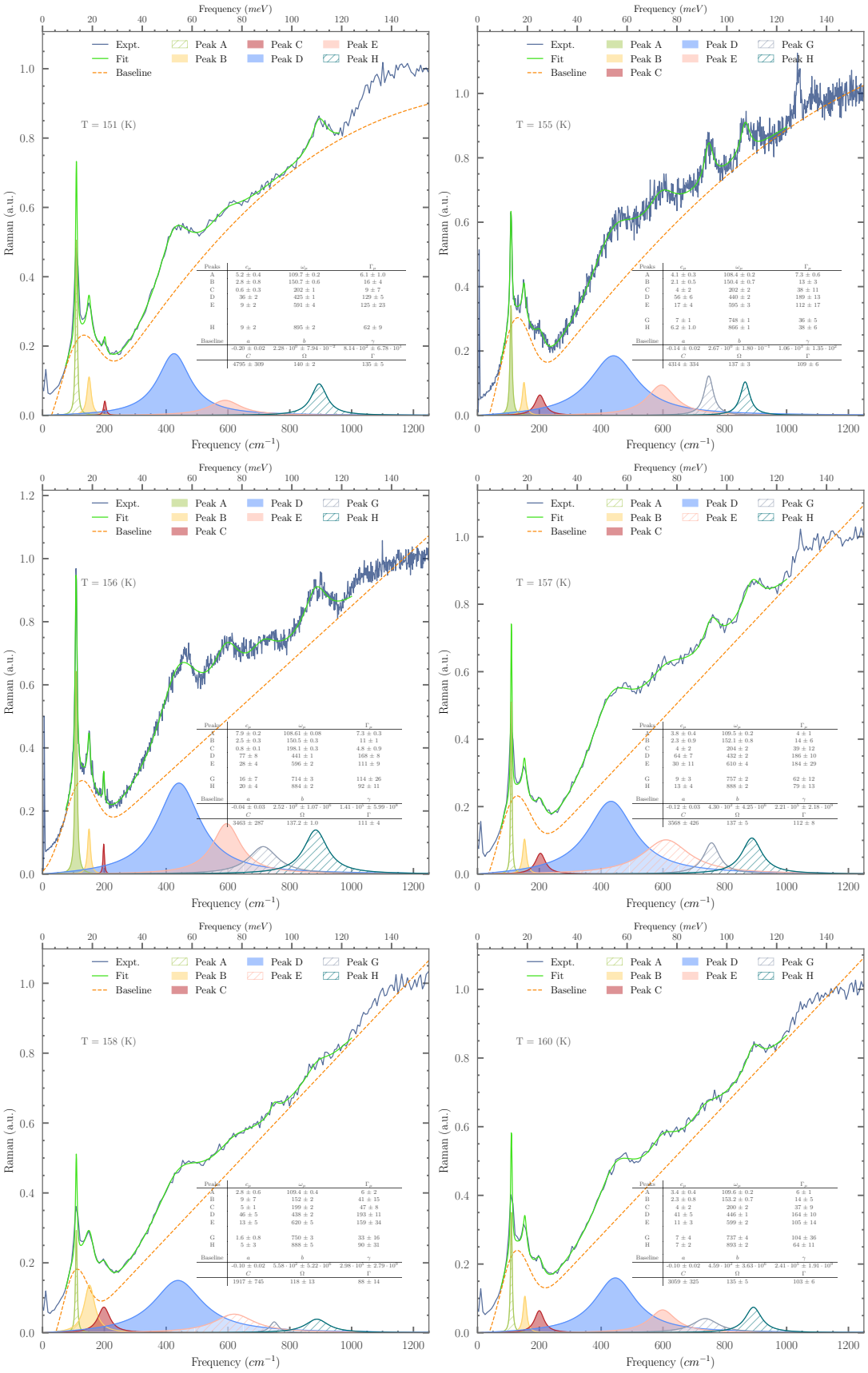
Frequency (meV)
Expt.
Fit
Baseline
Peak A
Peak B
Peak C
Peak D
Peak E
Peak G
Peak H
T = 151 (K)
T = 155 (K)
T = 156 (K)
T = 157 (K)
T = 158 (K)
T = 160 (K)
Raman (a.u.)
Frequency (cm^{-1})

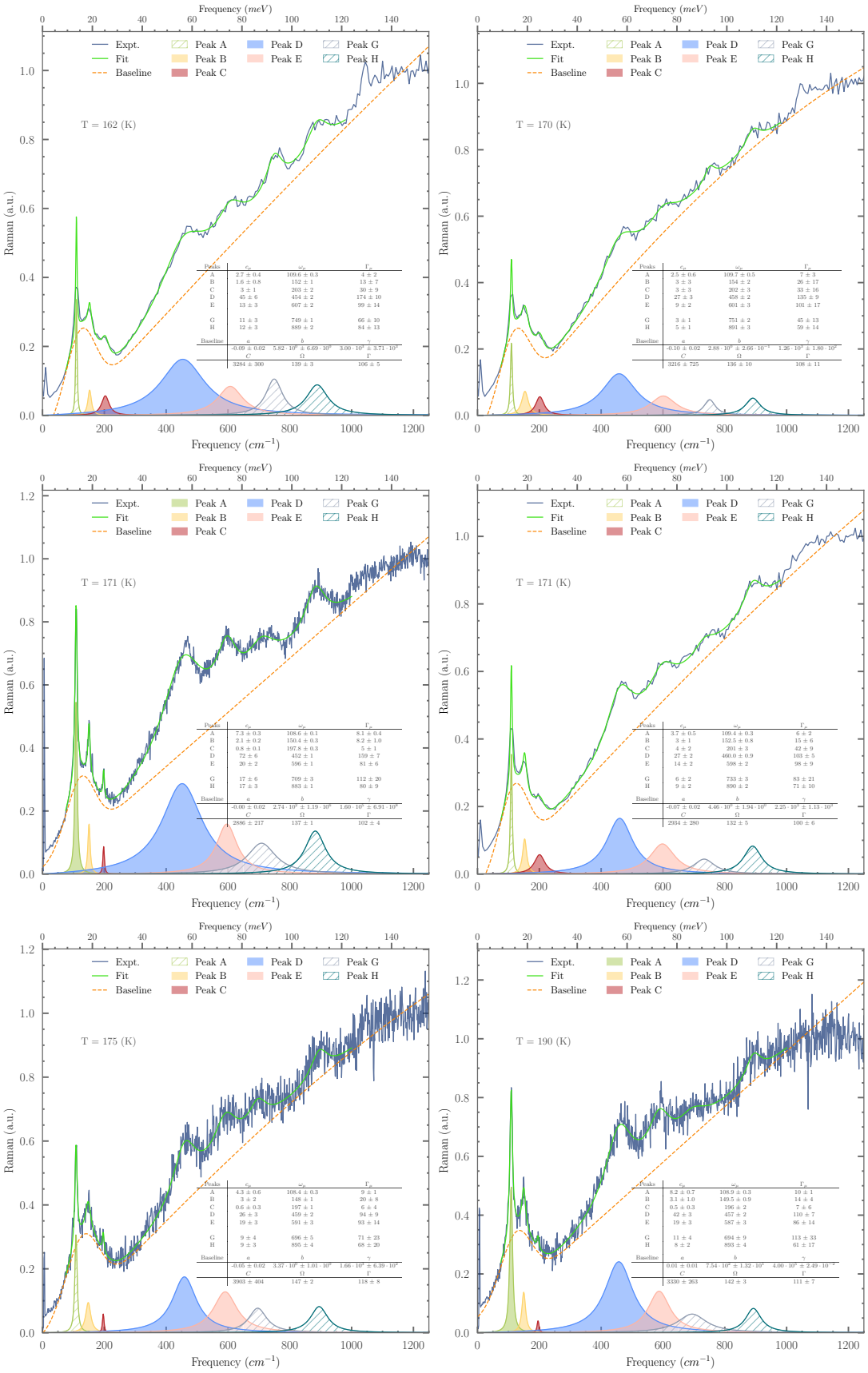
Frequency (meV)
Expt.
Fit
Baseline
Peak A
Peak B
Peak C
Peak D
Peak E
Peak G
Peak H
T = 162 (K)
T = 170 (K)
T = 171 (K)
T = 171 (K)
T = 175 (K)
T = 190 (K)
Raman (a.u.)
Frequency (cm^{-1})

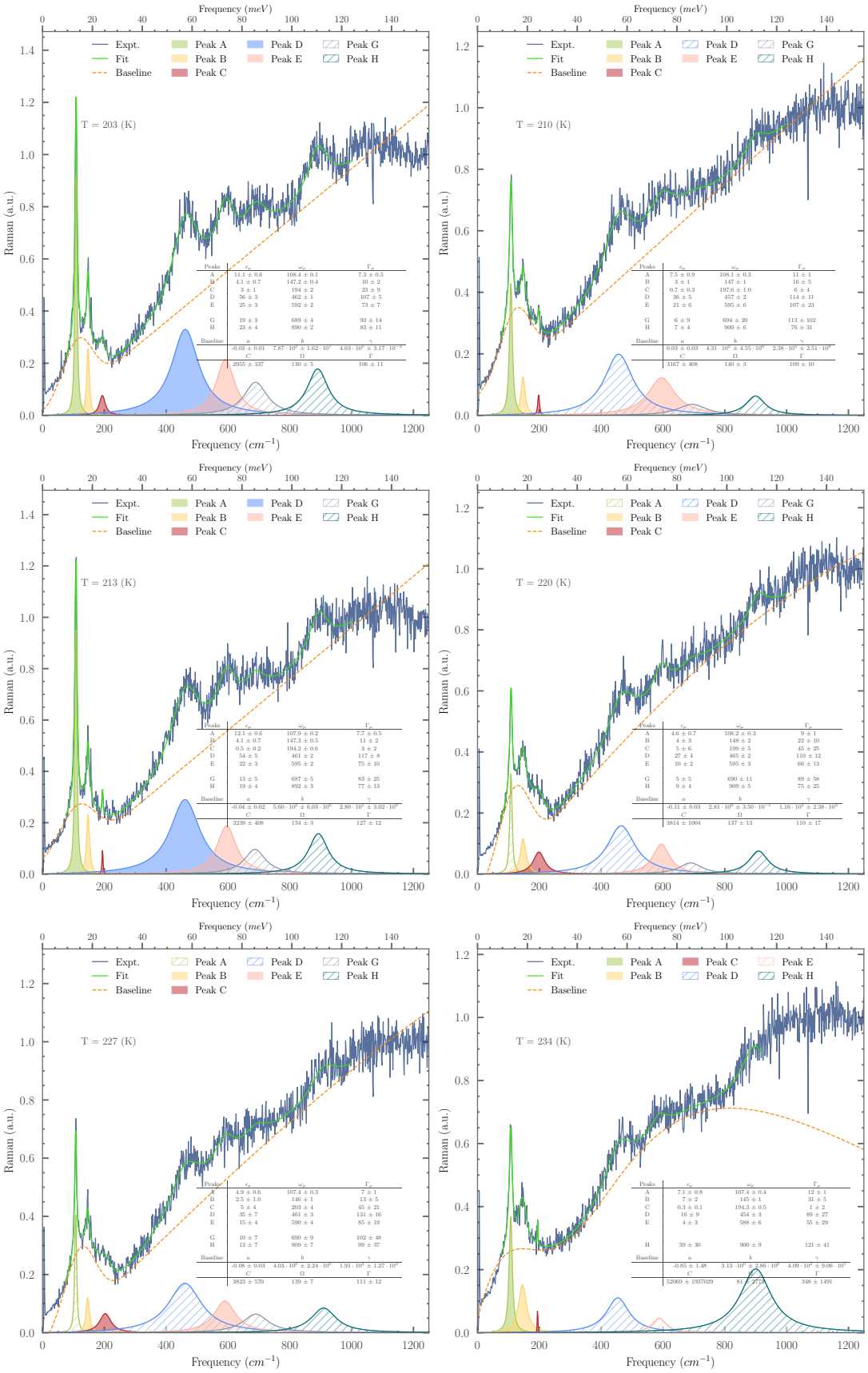
Frequency (meV)
Expt.
Fit
Baseline
Peak A
Peak B
Peak C
Peak D
Peak E
Peak G
Peak H
T = 203 (K)
T = 210 (K)
T = 213 (K)
T = 220 (K)
T = 227 (K)
T = 234 (K)
Raman (a.u.)
Frequency (cm^{-1})

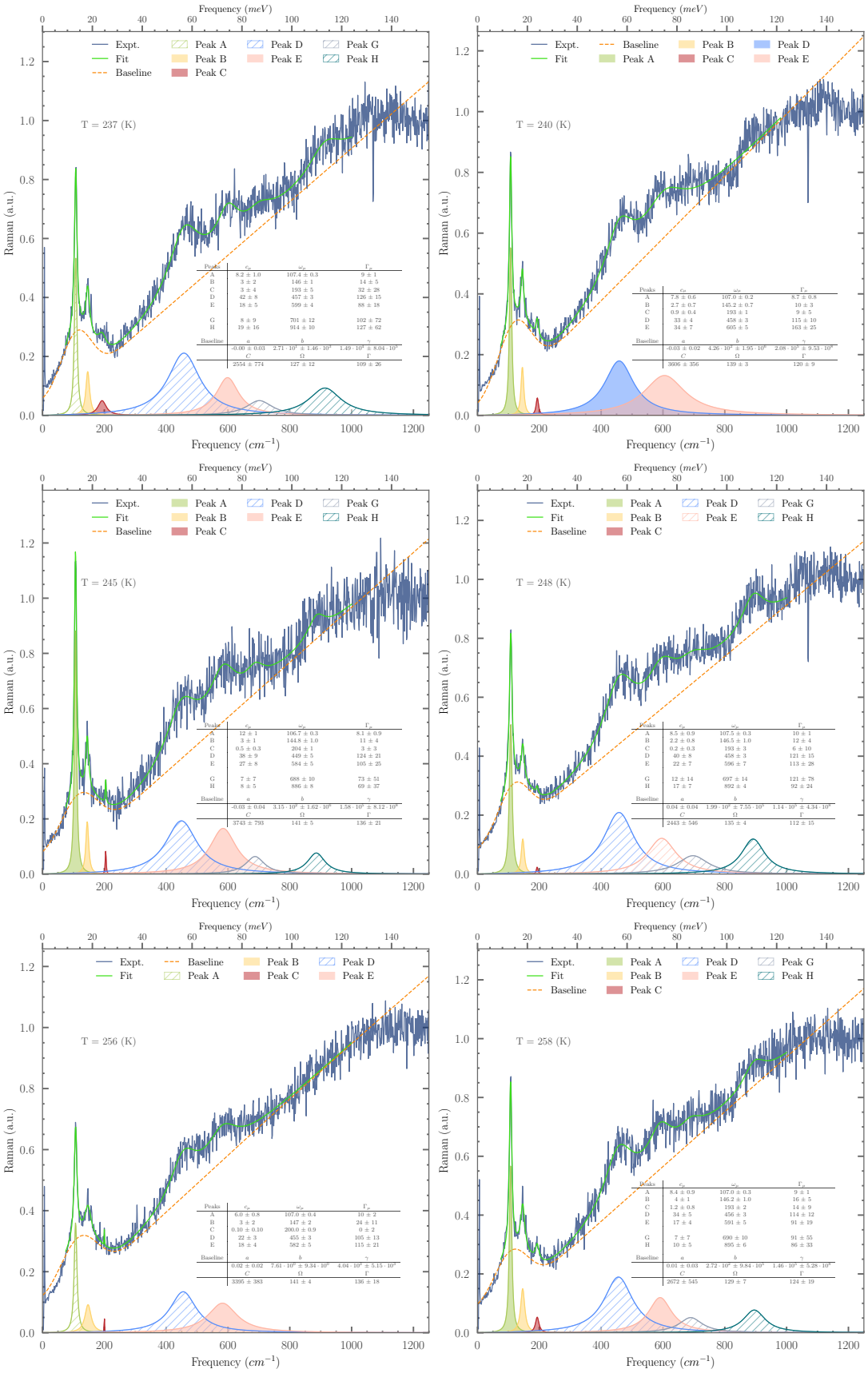
Frequency (meV)
Raman (a.u.)
Frequency (cm^{-1})
Expt.
Fit
Baseline
Peak A
Peak B
Peak C
Peak D
Peak E
Peak G
Peak H
T = 237 (K)
T = 240 (K)
T = 245 (K)
T = 248 (K)
T = 256 (K)
T = 258 (K)

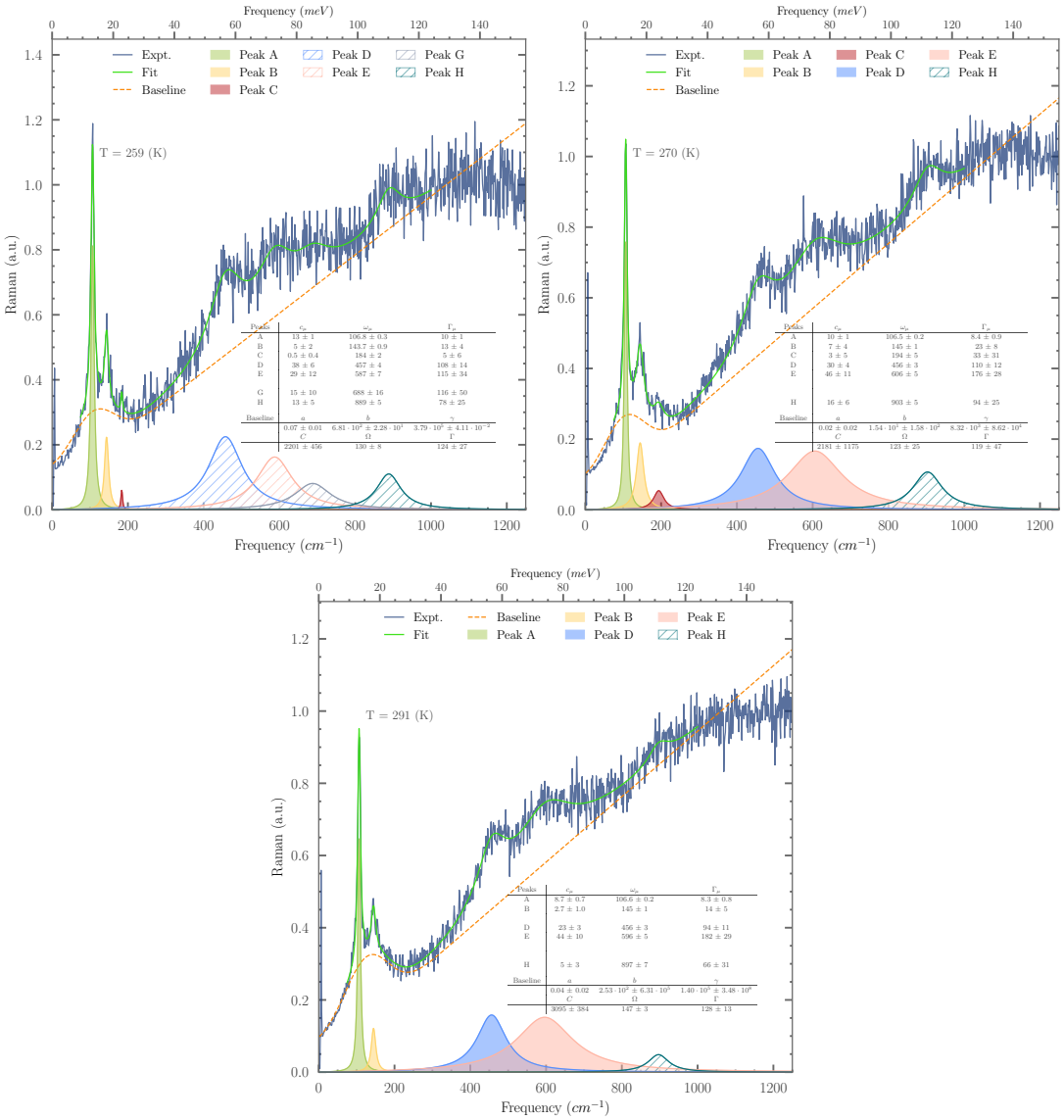
Frequency (meV)
Expt.
Fit
Baseline
Peak A
Peak B
Peak C
Peak D
Peak E
Peak G
Peak H
T = 259 (K)
T = 270 (K)
T = 291 (K)
Raman (a.u.)
Frequency (cm^{-1})

B Spectra sample 2

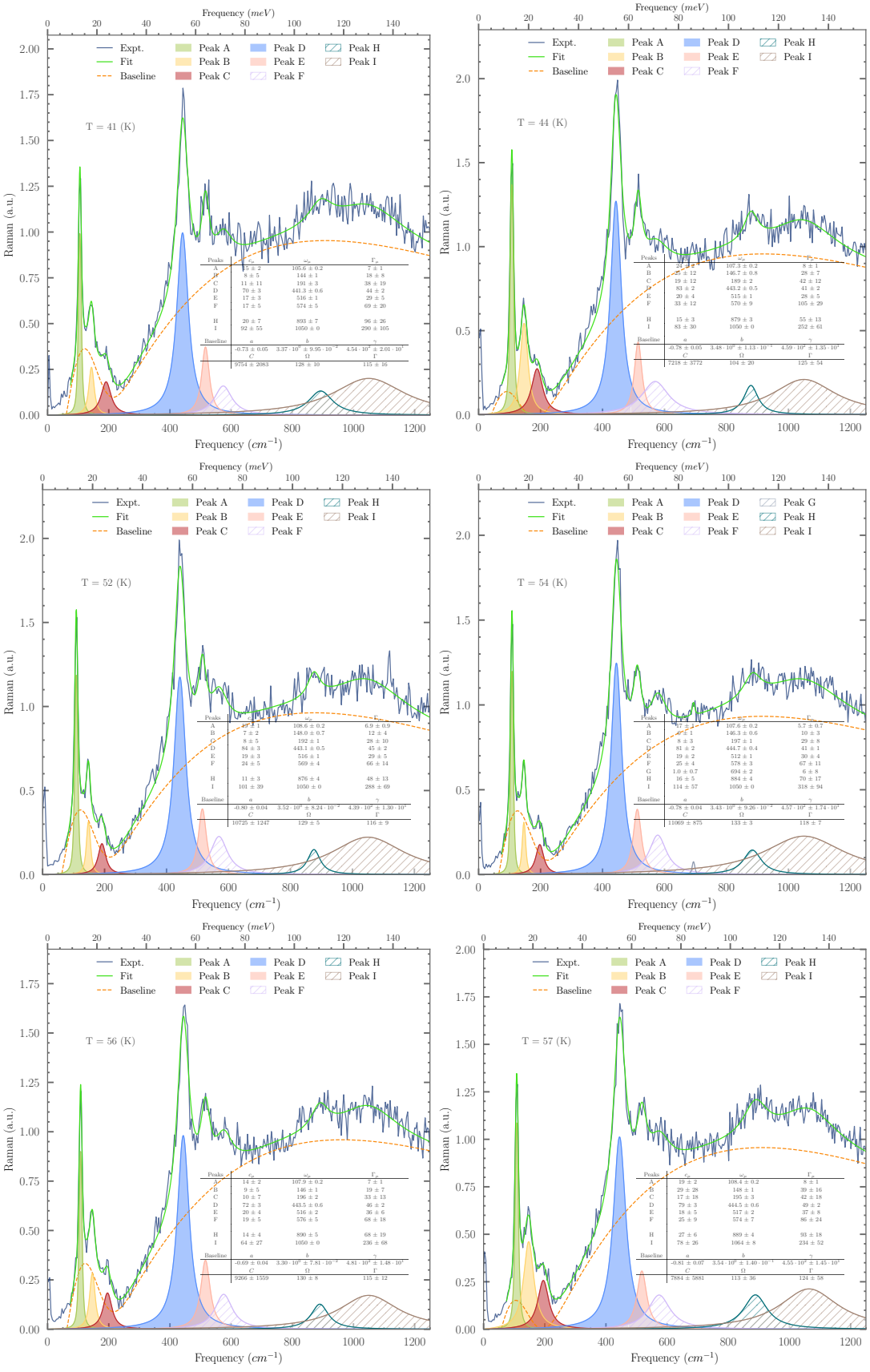
Frequency (meV)
Frequency (cm^{-1})
Raman (a.u.)
Expt.
Fit
Baseline
Peak A
Peak B
Peak C
Peak D
Peak E
Peak F
Peak G
Peak H
Peak I
T = 41 (K)
T = 44 (K)
T = 52 (K)
T = 54 (K)
T = 56 (K)
T = 57 (K)

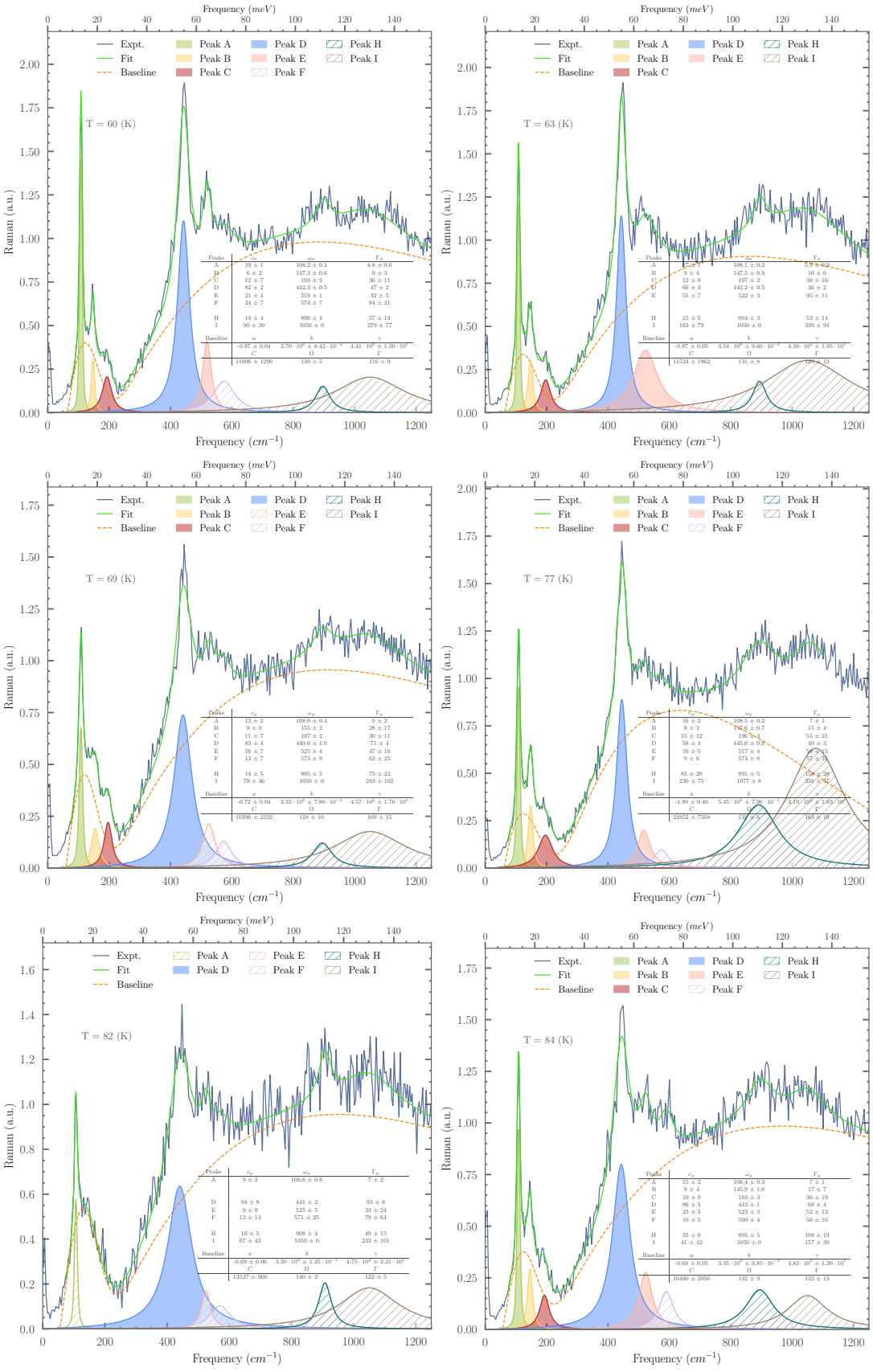
Frequency (meV)
Frequency (cm^{-1})
Raman (a.u.)
Expt.
Fit
Baseline
Peak A
Peak B
Peak C
Peak D
Peak E
Peak F
Peak H
Peak I
T = 60 (K)
T = 63 (K)
T = 69 (K)
T = 77 (K)
T = 82 (K)
T = 84 (K)

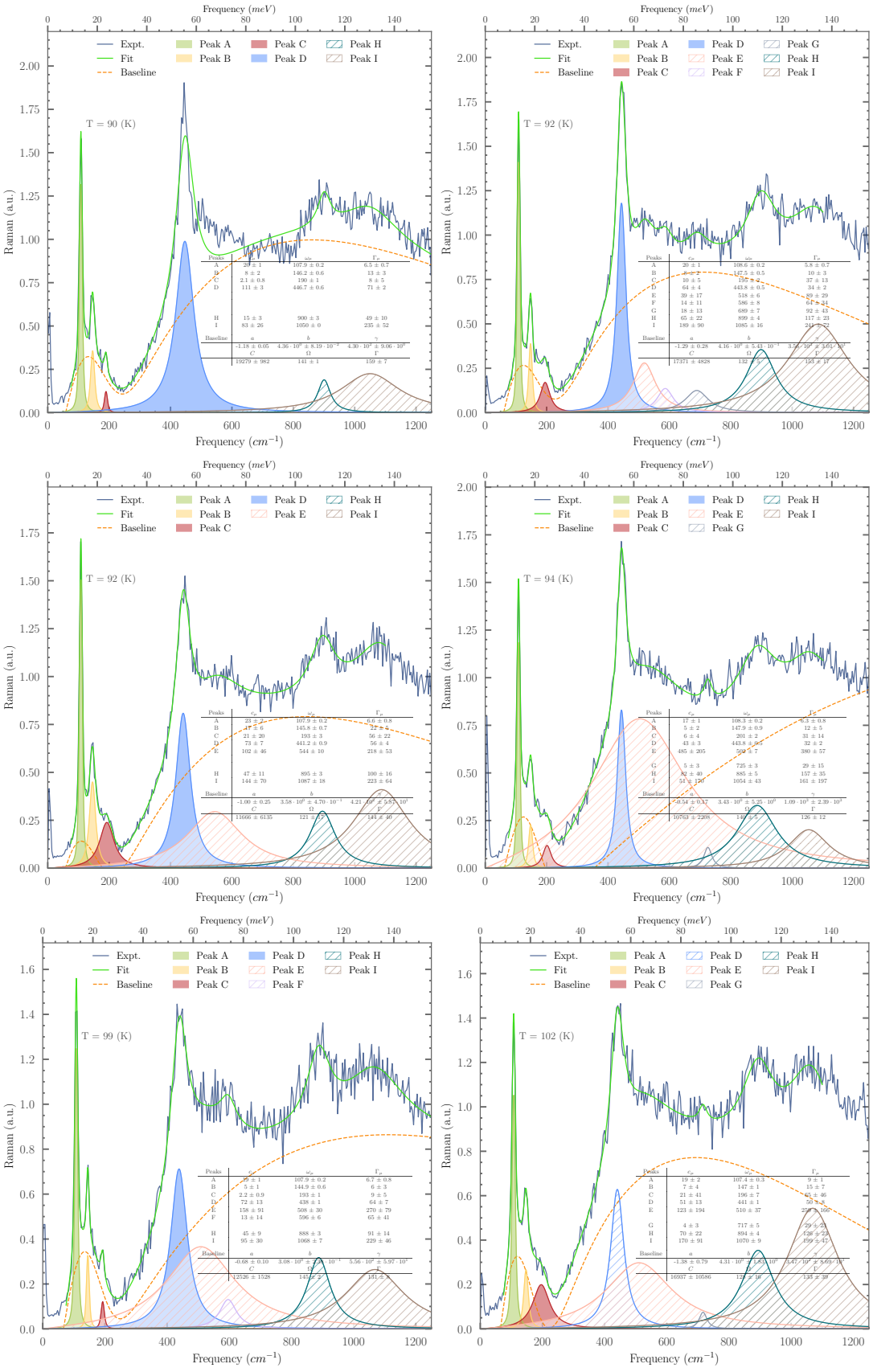
Frequency (meV)
Expt.
Fit
Baseline
Peak A
Peak B
Peak C
Peak D
Peak E
Peak F
Peak G
Peak H
Peak I
T = 90 (K)
T = 92 (K)
T = 92 (K)
T = 94 (K)
T = 99 (K)
T = 102 (K)
Raman (a.u.)
Frequency (cm^{-1})

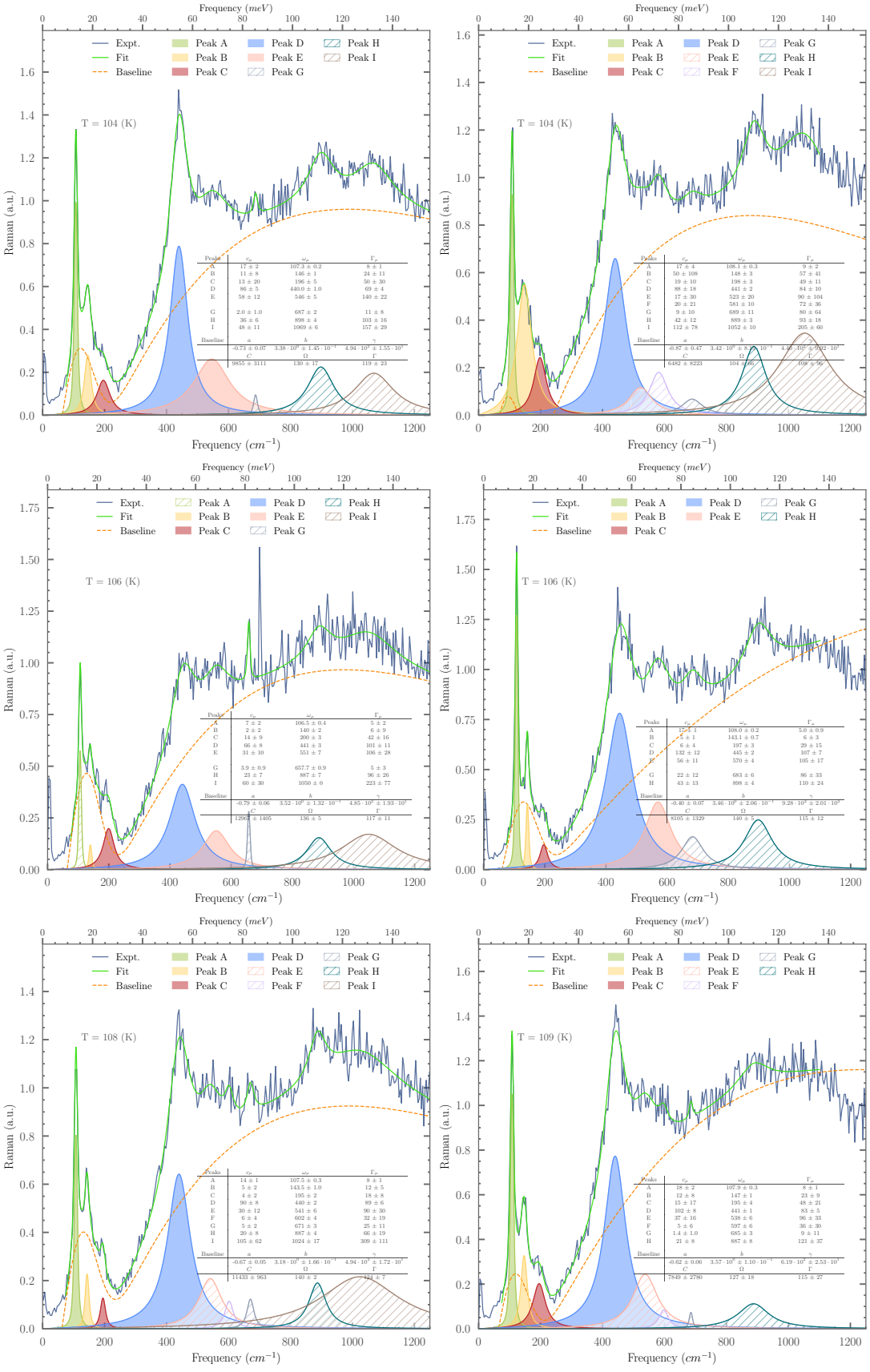
Frequency (meV)
Frequency (cm^{-1})
Raman (a.u.)
Expt.
Fit
Baseline
Peak A
Peak B
Peak C
Peak D
Peak E
Peak F
Peak G
Peak H
Peak I
T = 104 (K)
T = 104 (K)
T = 106 (K)
T = 106 (K)
T = 108 (K)
T = 109 (K)

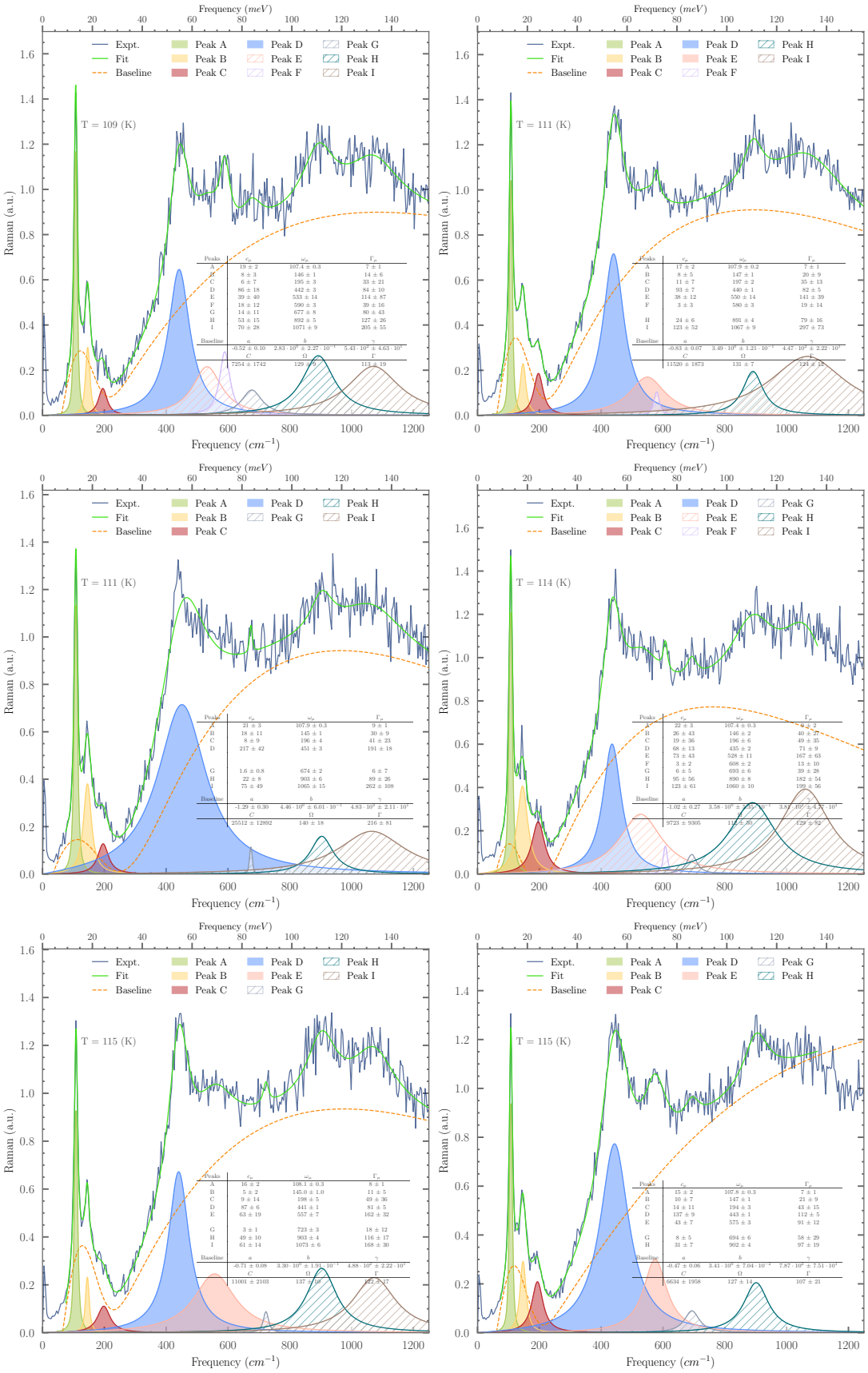
Frequency (meV)
Expt.
Fit
Baseline
Peak A
Peak B
Peak C
Peak D
Peak E
Peak F
Peak G
Peak H
Peak I
T = 109 (K)
T = 111 (K)
T = 111 (K)
T = 114 (K)
T = 115 (K)
T = 115 (K)
Raman (a.u.)
Frequency (cm^{-1})

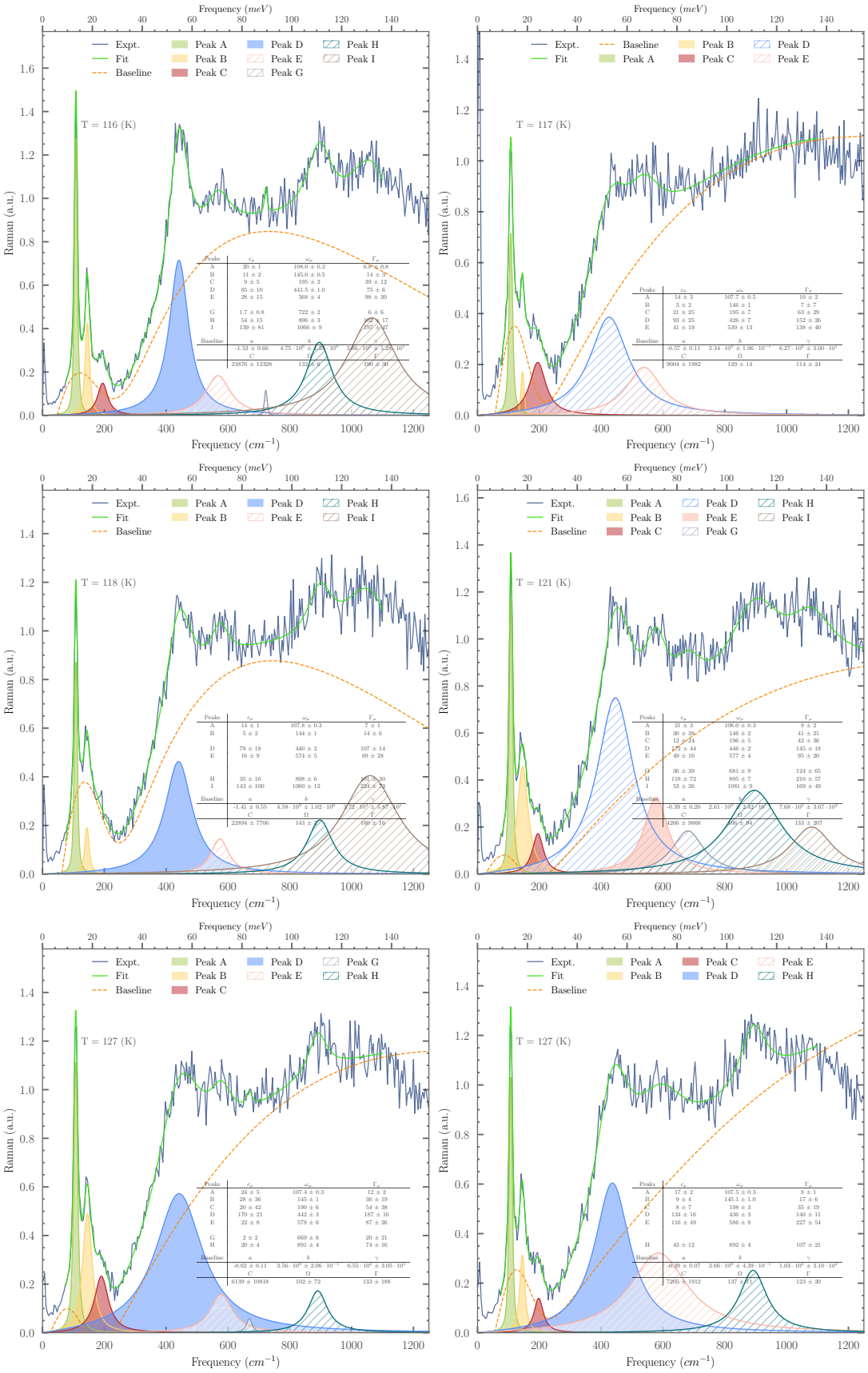
Frequency (meV)
Expt.
Fit
Baseline
Peak A
Peak B
Peak C
Peak D
Peak E
Peak G
Peak H
Peak I
T = 116 (K)
T = 117 (K)
T = 118 (K)
T = 121 (K)
T = 127 (K)
T = 127 (K)
Raman (a.u.)
Frequency (cm^{-1})

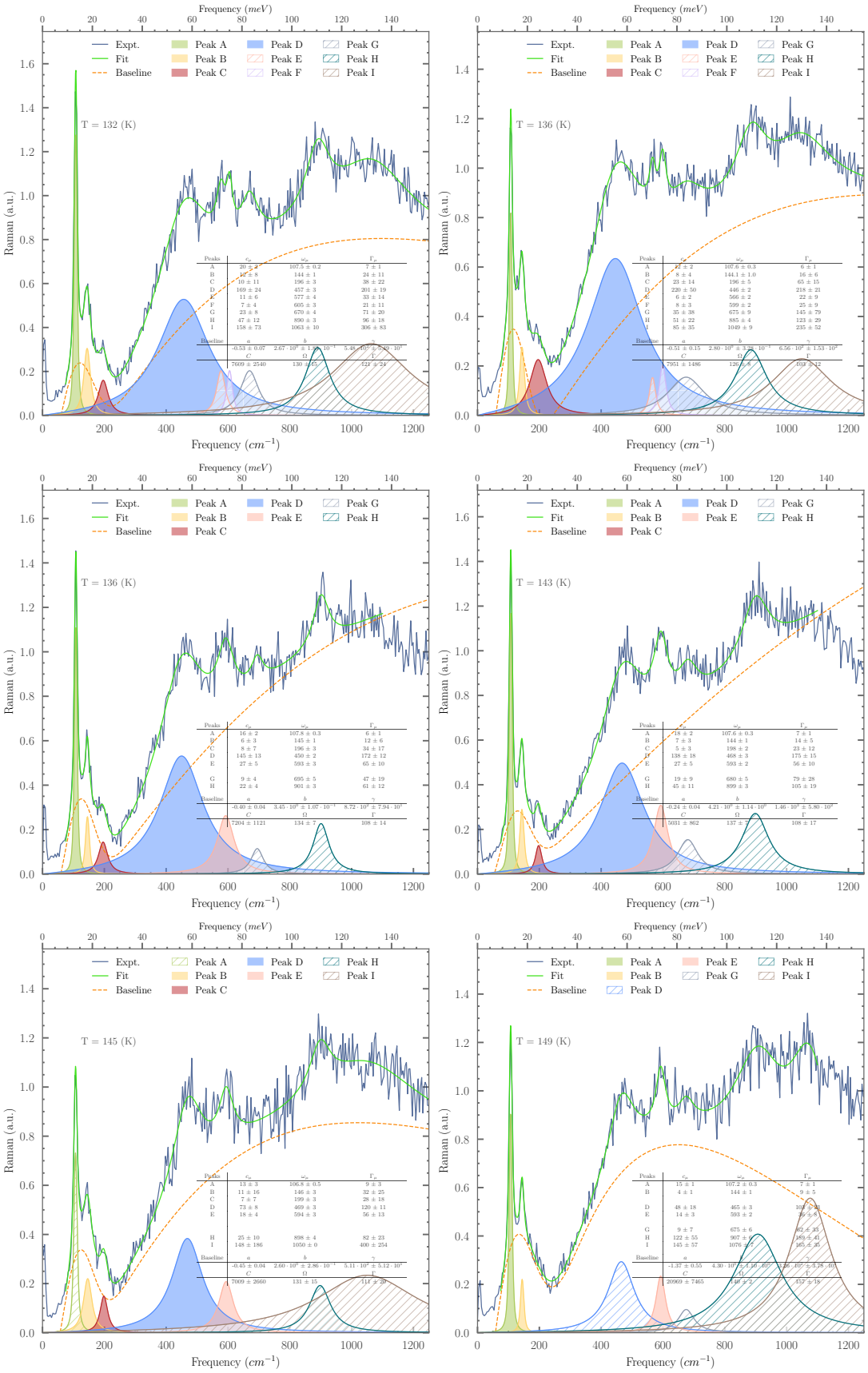
Frequency (meV)
Expt.
Fit
Baseline
Peak A
Peak B
Peak C
Peak D
Peak E
Peak F
Peak G
Peak H
Peak I
T = 132 (K)
T = 136 (K)
T = 136 (K)
T = 143 (K)
T = 145 (K)
T = 149 (K)
Raman (a.u.)
Frequency (cm^{-1})

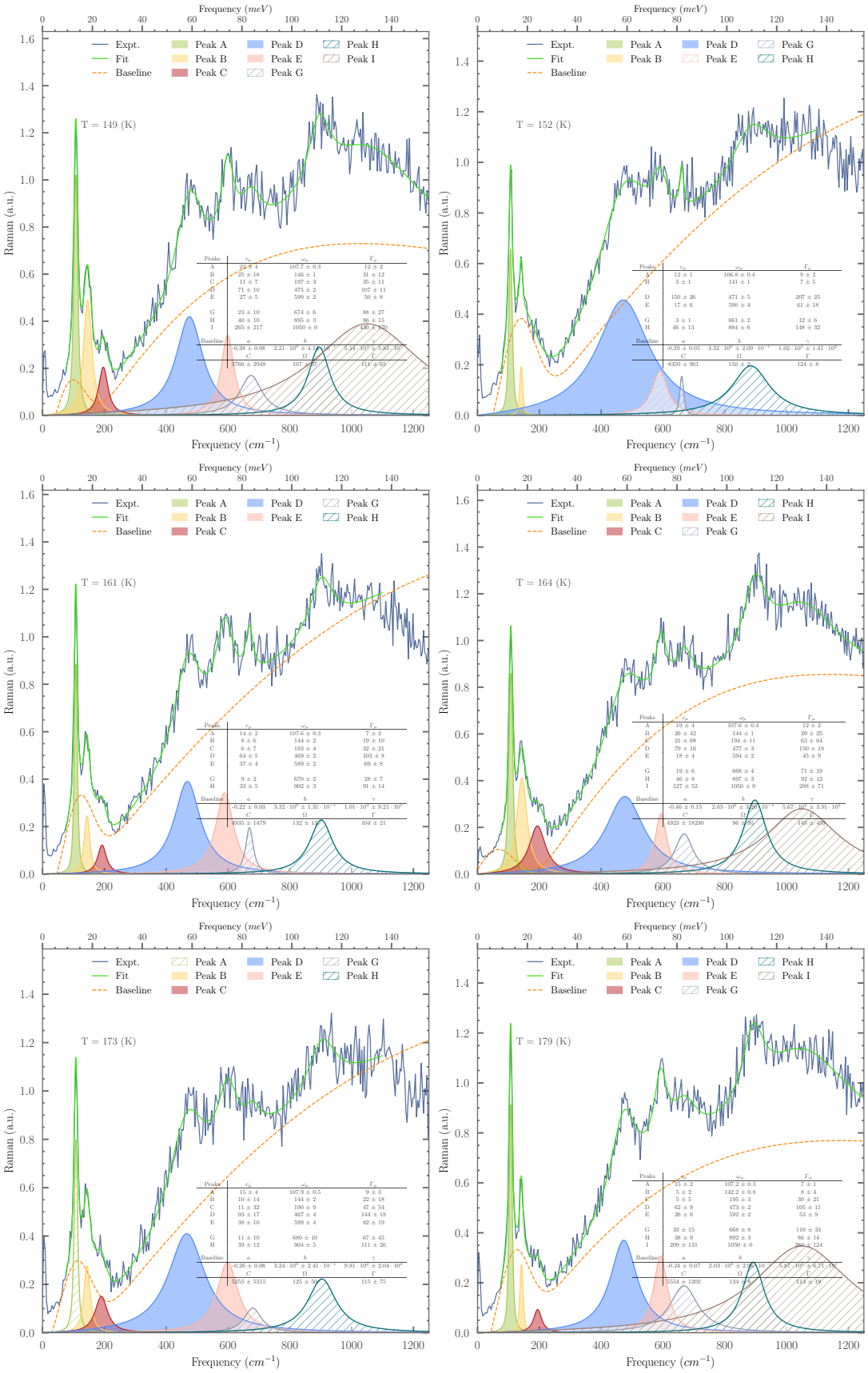
Frequency (meV)
Frequency (cm^{-1})
Raman (a.u.)
Expt.
Fit
Baseline
Peak A
Peak B
Peak C
Peak D
Peak E
Peak G
Peak H
Peak I
T = 149 (K)
T = 152 (K)
T = 161 (K)
T = 164 (K)
T = 173 (K)
T = 179 (K)

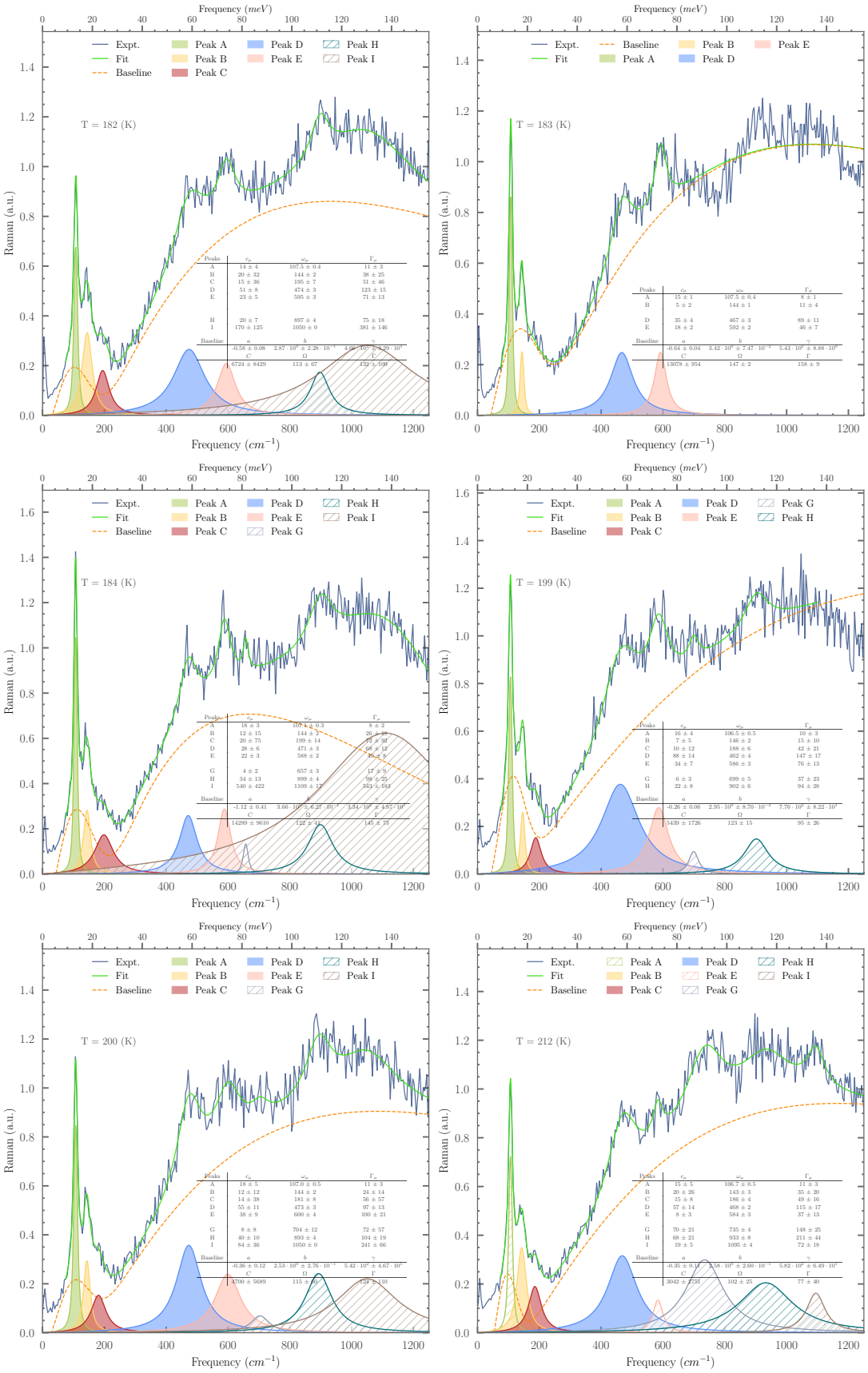
Frequency (meV)
Expt.
Fit
Baseline
Peak A
Peak B
Peak C
Peak D
Peak E
Peak G
Peak H
Peak I
T = 182 (K)
T = 183 (K)
T = 184 (K)
T = 199 (K)
T = 200 (K)
T = 212 (K)
Raman (a.u.)
Frequency (cm^{-1})

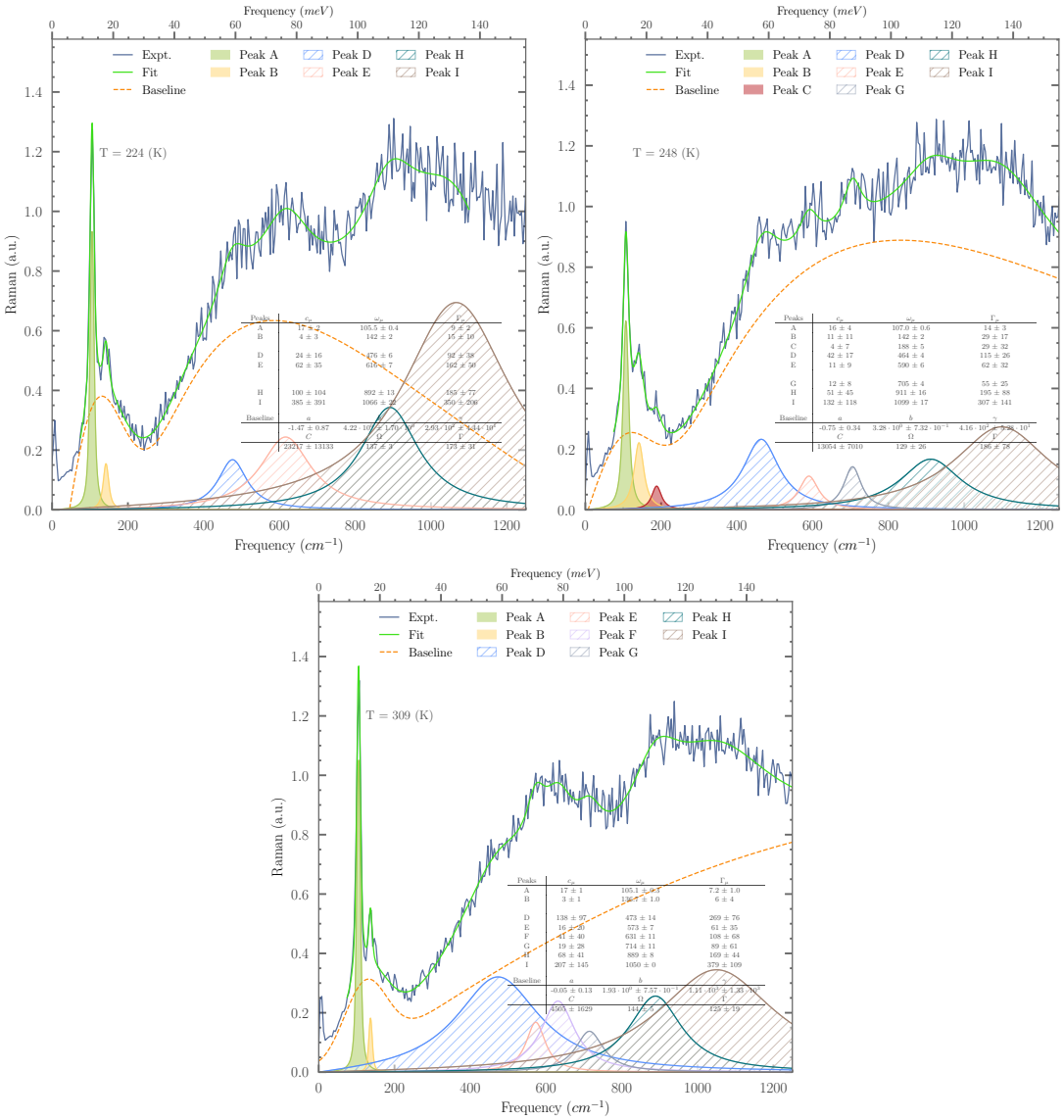
Frequency (meV)
Expt.
Fit
Baseline
Peak A
Peak B
Peak D
Peak E
Peak H
Peak I
T = 224 (K)
Raman (a.u.)
Frequency (cm^{-1})
Peak C
Peak G
T = 248 (K)
T = 309 (K)
Peak F